KeAi

CHINESE ROOTS
GLOBAL IMPACT

Contents lists available at ScienceDirect

Petroleum Science

journal homepage: www.keaipublishing.com/en/journals/petroleum-science



Original Paper

A new model for determining the effective permeability of tight reservoirs based on Fractal-Monte Carlo method



You Zhou a, b, Song-Tao Wu b, *, Ru-Kai Zhu b, Xiao-Hua Jiang b, Gan-Lin Hua c

- ^a School of Civil Engineering, Hebei University of Engineering, Handan, 056038, Hebei, China
- ^b PetroChina Research Institute of Petroleum Exploration & Development, Beijing, 100083, China
- ^c China Petroleum Enterprise Association, Beijing, 100120, China

ARTICLE INFO

Article history: Received 22 November 2024 Received in revised form 18 February 2025 Accepted 16 April 2025 Available online 24 April 2025

Edited by Jie Hao

Keywords: Tight reservoirs Boundary layer Permeability model Fractal theory Monte Carlo

ABSTRACT

In contrast to conventional reservoirs, tight formations have more complex pore structures and significant boundary layer effect, making it difficult to determine the effective permeability. To address this, this paper first proposes a semi-empirical model for calculating boundary layer thickness based on dimensional analysis, using published experimental data on microcapillary flow. Furthermore, considering the non-uniform distribution of fluid viscosity in the flow channels of tight reservoirs, a theoretical model for boundary layer thickness is established based on fractal theory, and permeability predictions are conducted through Monte Carlo simulations. Finally, sensitivity analyses of various influencing parameters are performed. The results show that, compared to other fractal-based analytical models, the proposed permeability probabilistic model integrates parameters affecting fluid flow with random numbers, reflecting both the fractal and randomness characteristics of capillary size distribution. The computational results exhibit the highest consistency with experimental data. Among the factors affecting the boundary layer, in addition to certain conventional physical and mechanical parameters, different microstructure parameters significantly influence the boundary layer as well. A higher tortuosity fractal dimension results in a thicker boundary layer, while increases in pore fractal dimension, porosity, and maximum capillary size help mitigate the boundary layer effect. It is also observed that the permeability of large pores exhibits greater sensitivity to changes in various influencing parameters. Considering micro-scale flow effects, the proposed model enhances the understanding of the physical mechanisms of fluid transport in dense porous media.

© 2025 The Authors. Publishing services by Elsevier B.V. on behalf of KeAi Communications Co. Ltd. This is an open access article under the CC BY license (http://creativecommons.org/licenses/by/4.0/).

1. Introduction

The petroleum and natural gas resources in the tight conglomerate reservoirs of the Junggar Basin, China, are emerging as a critical source of unconventional fossil fuels, representing a significant type of tight oil and gas (Yang et al., 2019; Wu et al., 2021; Kuang et al., 2023). Statistics indicate that the conglomerate reservoirs in the Mahu Sag, located on the northwestern margin of the Junggar Basin, contain proven reserves exceeding 1.24 billion tons and rank among the largest conglomerate oil fields in the world (Yuan et al., 2024). Compared to conventional sandstone, conglomerate reservoirs display poor reservoir quality, rapid

To better understand the pore structure and flow behavior of tight conglomerate reservoirs, researchers have recently applied characterization methods traditionally used for conventional reservoirs. Methods like scanning electron microscope (SEM), mercury injection capillary pressure (MICP), micro/nano computed tomography (CT) scan, and nuclear magnetic resonance (NMR) are employed for qualitative or quantitative analysis of pore structures in conglomerates (Li et al., 2022; Li et al., 2023a; Yu et al., 2023a;

Peer review under the responsibility of China University of Petroleum (Beijing).

physical property changes, pronounced heterogeneity, and significantly complex pore structures (Tian et al., 2019; Wang et al., 2022; Xiao et al., 2021). As development in the Mahu Sag advances, several production challenges have become evident, such as substantial variations in production across reservoir types, significant differences in single-well output, and low recovery efficiency (Ablimit et al., 2016; Li et al., 2020). Thus, an in-depth investigation of the pore structure and flow characteristics of these reservoirs is crucial to improving development efficiency in this region.

^{*} Corresponding author.

E-mail addresses: wust@petrochina.com.cn, rock.geoscience@outlook.com (S.-T. Wu).

Zheng et al., 2023). Studies reveal that tight conglomerate reservoirs mainly consist of micropores, nanopores, and throats, with a highly uneven pore size distribution (Peng et al., 2024). It should be noted that due to the wide range of particle sizes in conglomerates, these qualitative methods struggle to effectively balance resolution and field of view. To address this issue, researchers have utilized modular automated processing system (MAPS) techniques for high-precision characterization (Du et al., 2021; Zhang et al., 2023), partially mitigating the challenges of balancing resolution and scale in traditional qualitative experiments.

Extensive research also confirms that the flow patterns in tight reservoirs differ from those in conventional oil and gas reservoirs (Abbasi et al., 2014; Behmanesh et al., 2018; Kulga and Ertekin, 2018). Wang and Fu (2021) found that in micro and nano-scale pores, solid-liquid effects resulting from molecular interactions between solids and liquids are significant. Fluid molecules are adsorbed onto pore surfaces, forming immobile boundary layers that reduce the flow radius and may even completely block throats. Therefore, in tight reservoirs, where pore throat sizes are primarily at the micro and nano-scale, the boundary layer significantly influences flow behavior. Generally, microscale flow research methods are used to study the microscopic seepage characteristics of low-permeability reservoirs. Experimental findings consistently show that boundary layer thickness is influenced by pressure gradients, fluid viscosity, pore radius, and fluid type, with these effects becoming more significant as pore size decreases (Tian et al., 2014). Li et al. (2011) found that in quartz capillaries with a radius of 2.5 µm, the boundary layer thickness can occupy more than 50% of the entire flow space, resulting in nonlinear flow characteristics in microtubes, which become more pronounced as the tube diameter decreases.

However, the boundary layer effect, a critical factor in tight conglomerate reservoirs, has not received sufficient attention in existing studies, hindering a comprehensive understanding of fluid flow behavior (Tan et al., 2022; Yu et al., 2023b). Several factors contribute to this issue. First, high-precision microscale flow experiments are expensive and time-consuming, which has led many existing permeability models to exclude boundary layer effect, resulting in inaccuracies in practical applications, especially for tight reservoirs (Zhou et al., 2021). Second, the thickness of the boundary layer is usually determined experimentally. However, existing formulas for calculating this thickness are entirely empirical, relying on three to four fitting constants, with insufficient explanatory analysis of the seepage phenomena underlying these constants (Chen et al., 2022b). Third, limitations in instrumentation, materials, and detection methods lead to significant variation in empirical expressions for boundary layer thickness derived by different researchers. These expressions are often complex and have limited applicability (Huang, 2022).

As previously mentioned, thoroughly investigating the nonlinear flow characteristics of fluids in tight reservoirs requires accurate characterization of the pore structure as a primary task (Li et al., 2023b; Guo et al., 2024). However, conglomerate reservoirs exhibit diverse pore space scales, strong heterogeneity, and disordered internal pore distributions, resulting in complex and variable flow channels. This poses significant challenges to relevant research efforts. Fortunately, fractal theory offers an effective approach to characterizing the pore structure of porous media, greatly simplifying the complexity of the pore space, and it has been extensively applied to predict the permeability of porous media (Yu and Cheng, 2002; Cai et al., 2020; Xiao et al., 2020). It is worth noting that although many studies have confirmed the fractal characteristics of coal (Zhang et al., 2024b), shale (Wang et al., 2025), sandstone (Liu

et al., 2024), and carbonate (Liu et al., 2022), whether the pore size distribution in conglomerates adheres to a fractal law still requires further investigation. In fact, our previous research has shown that the pore space in the reservoirs of the Mahu region spans a wide range of scales, exhibiting a continuous distribution from the nanoscale to the microscale and up to the millimeter scale, with strong heterogeneity. The pore size distribution exhibits multifractal (Zhou et al., 2018) and intermingled fractal characteristics (Zhou et al., 2021). This suggests that the complex and variable pore structure of conglomerates cannot be effectively simplified by mono-fractal theory, and using a single fractal dimension to characterize it would inevitably exclude a considerable amount of valuable information. In this context, incorporating the randomness of pore size distribution into traditional fractal theory is an innovative approach, known as the Fractal-Monte Carlo Method (FMCM). The theoretical foundation lies in the fact that pore sizes follow both mono/multi-fractal scaling laws and random spatial distributions within the medium. Yu et al. (2005) were the first to combine fractal theory of porous media with the Monte Carlo method to simulate the permeability of porous media. They found that the permeability results obtained using FMCM matched experimental measurements well. This method combines the advantages of analytical analysis and numerical simulation, offering an effective tool for detailed characterization of the microstructure of porous materials. Since then, this innovative approach has been successfully applied to other specialized fields in oil and gas field development (Chen et al., 2022a; Shang et al., 2019; Yin et al., 2022). Zhang et al. (2024a) proposed a new analytical model for calculating the K-C constant based on FMCM, and found that the K-C constant increases with relative roughness, porosity, pore fractal dimension, and tortuosity fractal dimension, while decreasing with capillary diameter and Knudsen number. Xu et al. (2023) reconstructed the random microstructure of fibrous porous materials based on FMCM and simulated single-phase fluid flow with the finite element method. They found that the predicted permeability values were in excellent agreement with empirical formulas. Xiao et al. (2012) proposed a relative permeability model for porous media using FMCM, and found that the phase fractal dimension is largely dependent on porosity. For fractal shale reservoirs, Yang et al. (2021) performed Monte Carlo simulations of gas flow, and the results showed that the apparent gas permeability of shale increased with the Knudsen number.

To date, the permeability model based on FMCM incorporating the boundary layer effect has not been reported. Furthermore, the existing empirical formulas for calculating boundary layer thickness have several limitations. First, the use of excessive empirical constants in these formulas restricts our understanding of the mechanisms behind microscopic seepage. Second, there is a lack of dimensional consistency among the various empirical equations, which arises from the fact that boundary layer theory is still in an exploratory and underdeveloped stage. When the fluid type changes, adjustments to the parameters may be required for curve refitting.

Given these issues, this study aims to reorganize and thoroughly analyze experimental data from the published literature. Using dimensional analysis, a new quantitative expression for calculating the thickness of the boundary layer is proposed, which has a broader applicability. Subsequently, a permeability prediction model for tight porous media based on FMCM is introduced, and its accuracy is validated by comparing with measured results. Finally, the factors influencing boundary layer thickness and permeability are quantitatively analyzed.

2. Theory of Fractal-Monte Carlo method for porous media

According to fractal geometry, the number of pores within the interval λ to $\lambda + d\lambda$ is given by the following equation (Yu and Li, 2001):

$$-dN = D_f \lambda_{\max}^{D_f} \lambda^{-(D_f+1)} d\lambda \tag{1}$$

where N represents the number of capillaries, and $D_{\rm f}$ is the pore fractal dimension. $\lambda_{\rm max}$ and λ represent the maximum pore diameter and an arbitrary pore diameter, respectively. The negative sign in Eq. (1) indicates that the number of pores decreases as pore diameter increases, reflecting a fundamental rule of fractal structures in nature. The probability density function (PDF) for the pore size distribution within porous media is given by (Yu et al., 2002):

$$f(\lambda) = D_f \lambda_{\min}^{D_f} \lambda^{-(D_f+1)} \tag{2}$$

where $f(\lambda)$ is the PDF and λ_{\min} denotes the minimum pore diameter. In two-dimensional space, $0 < D_f < 2$, while in three-dimensional space, $0 < D_f < 3$ ° According to probability theory, Eq. (1) should satisfy the normalization condition, given by:

$$\int_{\lambda_{\min}}^{\lambda_{\max}} f(\lambda) d\lambda = 1 - \left(\frac{\lambda_{\min}}{\lambda_{\max}}\right)^{D_f} \equiv 1$$
 (3)

The prerequisite for Eq. (3) to hold is as follows:

$$\left(\frac{\lambda_{\min}}{\lambda_{\max}}\right)^{D_f} \approx 0 \tag{4}$$

In general, porous media readily satisfy $\lambda_{min}/\lambda_{max} < 10^{-2}$, indicating that pore size distribution generally satisfies Eq. (4), allowing fractal theory to be applied in analyzing the properties of porous media. Based on Eq. (2), the cumulative distribution function (CDF) for pore size distribution within the range λ_{min} to λ can be obtained as follows:

$$R(\lambda) = \int_{\lambda_{min}}^{\lambda} f(\lambda) d\lambda = 1 - \left(\frac{\lambda_{min}}{\lambda}\right)^{D_f}$$
 (5)

where $R(\lambda)$ is the CDF. Using the inverse sampling method, Eq. (5) can be rewritten as:

$$\lambda = \frac{\lambda_{\min}}{(1 - R)^{1/D_{\rm f}}} \tag{6}$$

where R represents random number. For the i-th capillary or pore, Eq. (6) can be rewritten as:

$$\lambda_i = \frac{\lambda_{\min}}{(1 - R_i)^{1/D_f}} \tag{7}$$

where λ_i denotes the diameter of the i-th capillary, and R_i is the i-th random number between 0 and 1. Eq. (7) represents the probability model for capillaries or pores, satisfying both randomness and the fractal scaling relationship. Here, i=1,2,3,...,J, where J is the total number of capillaries or pores generated in each Monte Carlo simulation under a given porosity. The fractal dimension in Eq. (7) is determined as follows (Yu et al., 2002):

$$D_{\rm f} = d - \frac{\ln \phi}{\ln \left(\frac{\lambda_{\rm min}}{\lambda_{\rm max}}\right)} \tag{8}$$

where ϕ is the effective porosity of the porous medium, and d is the Euclidean dimension (with d=2 and d=3 representing two- and three-dimensional spaces, respectively). Eq. (1) through Eq. 8 establish the theoretical foundation for using FMCM to simulate pore size distribution (Yu, 2016).

It should be noted that in describing transport properties of porous media using fractal theory, a cubic representative unit cell is often used for analysis. Here, we take a two-dimensional fractal porous medium as an example. Assuming that the set of pores following a fractal distribution is distributed across a unit cell, the total cross-sectional area of this unit cell is given by:

$$A_{t} = \frac{A_{p}}{\phi} = \frac{\int_{\lambda_{\min}}^{\lambda_{\max}} \frac{\pi}{4} \lambda^{2} (-dN)}{\phi} = \frac{\frac{\pi D_{f} \lambda_{\max}^{2}}{4(2-D_{f})} \left[1 - \left(\frac{\lambda_{\min}}{\lambda_{\max}}\right)^{2-D_{f}}\right]}{\phi}$$
(9)

where A_t and A_p represent the total area and the pore area of the unit cell, respectively. By substituting Eq. (8) into Eq. (9), we obtain:

$$L_0 = \sqrt{A_t} = \sqrt{\frac{1 - \phi}{\phi} \cdot \frac{\pi D_f \lambda_{\text{max}}^2}{4(2 - D_f)}}$$
 (10)

where L_0 is the side length of the square cell. Note that $A_{\rm t}$ does not typically represent the actual area of a sample, nor does L_0 represent its actual length.

3. Semi-empirical formula for calculating boundary layer thickness

The tortuous capillary model that considers boundary layer effect is shown in Fig. 1. Accurately measuring the thickness of the adsorption layer is challenging. Previous expressions for this thickness are curve-fitting models derived from extensive microcapillary experimental data. As a result, the applicability of these formulas is quite limited. Among them, the most representative computational formula was proposed by Tian et al. (2015), and it has been widely adopted by other researchers (Cao et al., 2016; Wang et al., 2017). Based on experimental results and dissipative particle dynamics (DPD) simulations, and considering factors such as fluid viscosity, capillary radius, and pressure gradient, the following equation is proposed (Tian et al., 2015):

$$h = r \cdot \beta_1 e^{\beta_2 r} (\nabla p)^{\beta_3} \cdot \mu \tag{11}$$

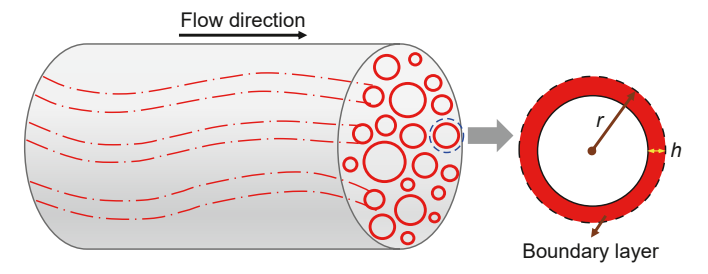


Fig. 1. Schematic of the tortuous capillary tube model coupling boundary layer effect.

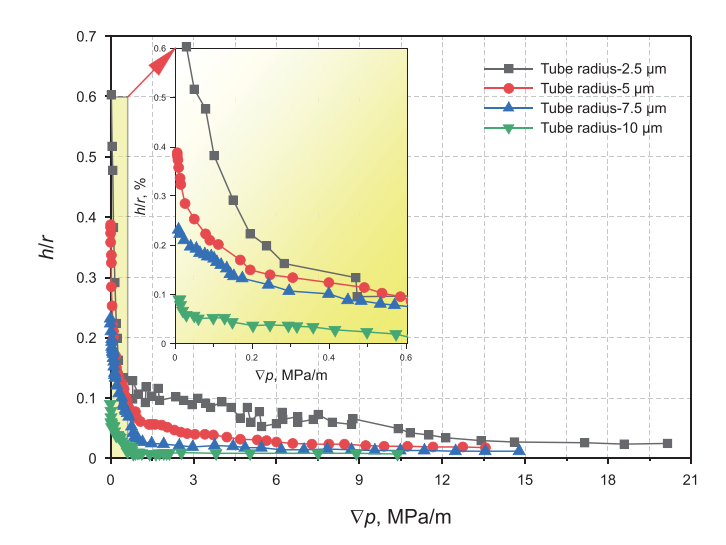


Fig. 2. Ratio of boundary layer thickness to tube radius vs. pressure gradient from experiments by Li et al. (2011).

where h is the boundary layer thickness in μ m, r is the pore radius in μ m, ∇p is the pressure gradient in MPa/m, μ is the fluid viscosity in mPa·s, β_1 , β_2 and β_3 are empirical constants that must be calibrated based on specific conditions. For deionized water, these constants are $\beta_1 = 0.25763$, $\beta_2 = -0.261$, and $\beta_3 = -0.419$ (Tian et al., 2016). Eq. (11) indicates that the thickness of the adsorption layer decreases as the pressure gradient increases, and for a fixed fluid type and pressure gradient, the ratio of boundary layer thickness to pore radius (h/r) increases as the pore radius decreases.

In this study, we conducted a detailed re-analysis of a substantial dataset from micro-capillary experiments in the published literature (Li and He, 2005; Liu et al., 2005; Xu et al., 2007; Li, 2010; Li et al., 2011). Among these, the experimental data from Li et al. (2011) is particularly comprehensive and has been widely cited in numerous studies, making it a valuable and reliable source for investigating factors influencing the thickness of the boundary layer (Fig. 2). Therefore, we selected this dataset for our analysis. For detailed experimental methods, setup, and testing procedures, please refer to Li et al. (2011).

Fig. 2 shows that the ratio of boundary layer thickness to capillary radius decreases as the pressure gradient increases. Under the same pressure gradient, smaller capillary radii result in a larger proportion of boundary fluid. When the pressure gradient exceeds 1 MPa/m, the thickness of the boundary fluid layer reaches a stable value. Under low-speed and low-pressure conditions, this thickness can account for more than 50% of the entire flow space.

Previous studies have shown that the boundary layer thickness h (μ m) is determined by the fluid dynamic viscosity μ (mPa·s), pressure gradient ∇p (MPa/m), and pore radius r. To obtain dimensionally consistent physical equations, we employed dimensional analysis to investigate the formula for calculating the thickness of boundary flow, incorporating fluid density ρ (g/cm³) into the analysis, as follows:

$$F(r, \mu, \rho, h, \nabla p) = 0 \tag{12}$$

Selecting r, μ , and ρ as the fundamental physical quantities, we have [r] = L, $[\mu] = ML^{-1}T^{-1}$, and $[\rho] = ML^{-3}$. According to the Π theorem yields:

$$F\left(\frac{h}{r}, \frac{\nabla p}{r^{-3}\mu^2\rho^{-1}}\right) = 0 \tag{13}$$

Let:

$$\zeta = \frac{\rho r^3 \nabla p}{1000\mu^2} \tag{14}$$

Then:

$$\frac{h}{r} = f\left(\frac{\rho r^3 \nabla p}{\mu^2}\right) = f(\zeta) \tag{15}$$

Eq. (15) indicates that the ratio of boundary layer thickness to tube radius is a function of the dimensionless number ζ . Considering that the pressure gradient is related to velocity v (m/s), we can also obtain a simpler form of the dimensionless number by rewriting Eq. (12) as:

$$F(r, \nu, \rho, \mu, h) = 0 \tag{16}$$

Similarly, by selecting r, v, and ρ as fundamental physical quantities, according to the Π theorem, we have:

$$F\left(\frac{h}{r}, \frac{\mu}{\rho \nu r}\right) = F\left(\frac{h}{r}, \frac{2}{Re}\right) = 0 \tag{17}$$

Thus:

$$\frac{h}{r} = f(Re) \tag{18}$$

Eq. (18) states that h/r depends solely on the Reynolds number *Re*. The above conclusions markedly harmonize the experimental findings from different researchers.

Fig. 3(a) and (b) demonstrate that as ζ or *Re* increases, the h/rprogressively decreases. Also, the smaller the tube radius, the steeper the curve becomes. This indicates that in smaller tubes, the thickness of the boundary layer exhibits greater sensitivity to dimensionless number ζ or *Re*. It is worth noting that, as shown in Fig. 2, the four curves follow different paths. In contrast, it can be observed that the four curves in Fig. 3(a) and (b) tend to converge, indicating that h/r is almost exclusively a function of the dimensionless number ζ or Re, thereby validating the reasonableness of Eqs. (15) and (18) to some extent. Additionally, Fig. 3(a) and (b) demonstrate that the experimental curves can be divided into two segments: a steep segment and a gentle one. This phenomenon is, in fact, a common characteristic of many microfluidic experiments, and we have observed similar trends in the experimental curves from numerous published studies (Li and He, 2005; Liu et al., 2005; Wang et al., 2011; Xiong et al., 2017; Xu et al., 2007). In the steep segment, the variation in boundary layer thickness is quite dramatic, intensifying the nonlinearity of the flow, which results in low-velocity non-Darcy seepage (Wang et al., 2020). The smaller ζ / Re, the greater the degree of non-linearity in the flow. This also explains why the degree of convergence of the four curves at low ζ / Re values is weaker than that at high levels. At lower ζ/Re levels, microscale flow effects such as solid-liquid interactions, starting pressure gradients, and wall roughness cannot be ignored, which increases the factors affecting h/r.

Subsequently, when the dimensionless number reaches a critical value and enters the gentle segment, the change in the thickness of boundary flow becomes smaller and tends to "solidify", causing the permeability of the porous media to stabilize at a nearly constant value. At this point, the flow enters a linear seepage phase, corresponding to Darcy flow (Ge et al., 2003). As the dimensionless number increases further, the flow naturally transitions into high-velocity non-Darcy flow, entering into the turbulent regime. However, it should be noted that the boundary between the steep and gentle segments in different experimental curves is not fixed but varies within a certain range. This is because, on one hand,

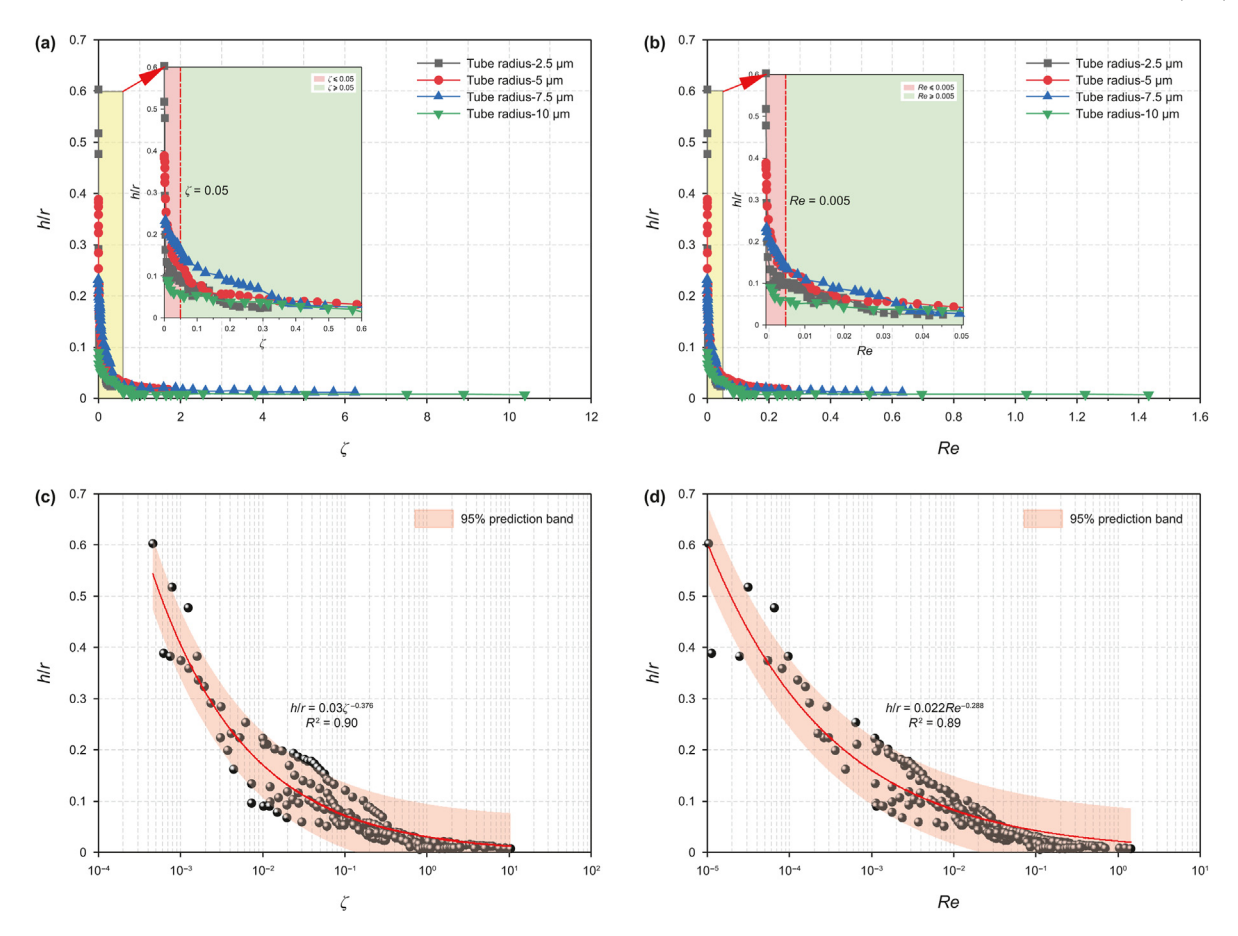


Fig. 3. Analysis of microscale flow experimental data by Li et al. (2011). (a) The relationship between *h/r* andζunder different tube radii; (b) The relationship between *h/r* and *Re* under different tube radii; (c) The nonlinear fitted relationship between *h/r* and *Re*.

different researchers may use varying experimental conditions and measurement methods, resulting in individual differences in the results. On the other hand, "steep" and "gentle" are qualitative observations. Therefore, it is not possible to provide an exact value for this critical point. In this experiment, we can roughly take $\zeta=0.05$ and Re=0.005 as the critical values. In this part, relevant experimental data can be found in Appendix A.

Fig. 3(c) and (d) show a negative correlation between h/r and the proposed dimensionless number. Based on this, we propose a semi-empirical formula for calculating the boundary layer thickness, as follows:

$$\frac{h}{r} = 0.03\zeta^{-0.376} \tag{19}$$

$$\frac{h}{r} = 0.022Re^{-0.288} \tag{20}$$

It can be seen that, except for a few outliers, likely caused by experimental errors, the majority of the data fall within the 95% prediction interval of the fitted formula. For practical applications, Eq. (19) is employed instead of Eq. (20) to calculate the thickness of the boundary layer. The reason is as follows.

Based on the definition of the Reynolds number:

$$Re = \frac{\rho \nu \lambda}{\mu} = \frac{2q(r)\rho}{\pi r \mu} \tag{21}$$

where q(r) represents the flow rate through a single capillary of radius r considering the effect of the boundary layer. This physical quantity is a function of h and r, as given by the modified Hagen-Poiseuille equation:

$$q(r) = \frac{\pi (r - h)^4 \Delta p}{8\mu L_t} \tag{22}$$

Here, L_t denotes the actual length of the curved capillary and Δp is the driving pressure difference. Substituting Eqs. (21) and (22) into Eq. (20) yields:

$$h = ar \left(\frac{2q(r)\rho}{\pi r\mu}\right)^b = ar \left(\frac{(r-h)^4 \rho \Delta p}{4\mu^2 r L_t}\right)^b$$
 (23)

where the values of a and b are 0.022 and -0.288, respectively. It is apparent that Eq. (23) is a higher-order implicit equation regarding the boundary layer thickness, which can only be solved numerically when the other parameters are fixed. However, due to its nonlinearity and implicit complexity, the numerical solution of this equation may exhibit instability or convergence difficulties at certain points. Therefore, for ease of application, we use Eq. (19) to calculate the thickness of the boundary layer. Note that when the pore radius is very small (when $\zeta < 8.9 \times 10^{-5}$), the calculated thickness of the adsorption layer will exceed the pore radius (Wang et al., 2017). In such cases, the capillary is entirely filled with a stagnant boundary layer, implying that h = r, and the effective liquid permeability of the capillary is zero.

It is important to highlight that the experimental data from Li et al. (2011) were obtained using quartz capillaries (with radii of 2.5, 5, 7.5, and 10 µm) and the flow medium was sterilized deionized water. However, on one hand, the size of most experimental tubes cannot reach the nanoscale, so the formulas of boundary layer thickness for a single capillary tube obtained from experimental studies may not be fully applicable. On the other hand, the pore throat structure of real rock cores is much more complex than the straight capillaries used in microscale flow experiments, and Eq. (19) cannot fully describe the influence of the pore structure on the boundary layer. Although in Section 5, we validated the reliability of Eq. (19) by comparing it with other published microscale flow experimental results, which showed that, compared with other purely empirical formulas, the predictions from our proposed formula demonstrated a stronger correlation with experimental measurements. However, in absolute terms, there is still some discrepancy, primarily due to differences between the experimental conditions and the actual pore structure, which is also a common issue for all curve-fitting formulas. Therefore, in practical applications, specific experiments need to be conducted based on the actual situation, and the empirical constants in Eq. (19) should be modified according to experimental results to better suit practical needs. Despite this, it still causes some inconvenience. To address this, in Section 4, we introduce a general permeability model that accounts for boundary layer effects and provide an analytical formula for calculating its thickness, which better reflects the impact of pore structure parameters on the boundary layer.

4. Permeability model considering boundary layer effect based on FMCM

4.1. Derivation of the theoretical formula

Considering that near solid walls, the attraction of the solid surface to water molecules causes a substantial increase in the viscosity of water close to the walls. Whereas far from solid surfaces, the solid-liquid effects are minimal, and the viscosity is similar to that of free water. Similarly, in flows involving crude oil, the oil components strongly interact with rock pore surfaces near the walls, leading to the adsorption of heavier and more polar substances. As the distance between the fluid and rock surfaces decreases, the concentration of fluid components increases, resulting in uneven distribution of oil viscosity within the pore throats. Therefore, substituting the inherent viscosity for the viscosity of the boundary fluid layer in microflows is clearly inappropriate. Actually, under low-speed and low-pressure conditions,

the capillary, with the r-axis extending from the center to the wall. In this case, r represents the distance from any point on the flow cross-section to the origin; μ is the viscosity at that point; r_0 denotes the capillary radius, and μ_0 represents the intrinsic viscosity of the fluid. Thus, the viscosity distribution within the capillary can be expressed as:

$$\mu = \frac{\mu_0 r_0}{r_0 - r} \tag{25}$$

Clearly, Eq. (25) also demonstrates that as the pore throat radius decreases, the uneven distribution of viscosity becomes more pronounced. Consider a capillary with an actual length $L_{\rm t}$, and take a liquid cylinder at a distance r from the center of the capillary as the research subject. Assuming it undergoes laminar flow under a driving pressure difference Δp with no acceleration, and that the driving force is balanced by the viscous resistance, as follows:

$$\pi r^2 \Delta P + \mu \cdot 2\pi r L_t \frac{\mathrm{d}v}{\mathrm{d}r} = 0 \tag{26}$$

The actual length of the curved capillary tube L_t is determined by Yu et al. (2014):

$$L_{t} = \lambda^{1-D_{T}} L_{0}^{D_{T}} = (2r)^{1-D_{T}} L_{0}^{D_{T}}$$
(27)

and

$$D_{\rm T} = 1 + \frac{\ln \tau_{\rm av}}{\ln \frac{L_0}{\lambda_{\rm cu}}} \tag{28}$$

Here, L_0 represents the straight or characteristic length along the direction of the macroscopic pressure gradient; D_T is the fractal dimension that describes the average degree of capillary curvature, known as the average tortuosity fractal dimension; $\lambda_{\rm av}$ is the average diameter of the capillaries, which can be determined by the mathematical expectation of λ :

$$\lambda_{\text{av}} = \int_{\lambda_{\text{min}}}^{\lambda_{\text{max}}} \lambda \cdot f(\lambda) d\lambda = \frac{D_{f} \lambda_{\text{max}}}{D_{f} - 1} \left[\frac{\lambda_{\text{min}}}{\lambda_{\text{max}}} - \left(\frac{\lambda_{\text{min}}}{\lambda_{\text{max}}} \right)^{D_{f}} \right]$$
(29)

Substituting Eq. (4) into Eq. (29) yields:

$$\lambda_{\text{av}} = \frac{D_{\text{f}} \lambda_{\text{min}}}{D_{\text{f}} - 1} \tag{30}$$

In addition, τ_{av} is the average tortuosity, which is determined by Yu and Li (2004):

$$\tau_{\text{av}} = \frac{1}{2} \left[1 + \frac{1}{2} \sqrt{1 - \phi} + \sqrt{1 - \phi} \sqrt{\left(\frac{1}{\sqrt{1 - \phi}} - 1 \right)^2 + \frac{1}{4}} / \left(1 - \sqrt{1 - \phi} \right) \right]$$
 (31)

the variation in fluid viscosity across the flow cross-section is a primary factor leading to nonlinear seepage. Based on this, we assumes that fluid viscosity near the wall approaches infinity, while at the center of the capillary, it matches the inherent viscosity, as follows:

$$\mu_{r=r_0} = \infty, \mu_{r=0} = \mu_0 \tag{24}$$

Note that the origin of the coordinate system is at the center of

Therefore, substituting Eqs. (25) and (27) into Eq. (26) yields:

$$\pi r^2 \Delta P + \frac{\mu_0 r_0}{r_0 - r} \cdot 2\pi r (2r)^{1 - D_T} L_0^{D_T} \frac{d\nu}{dr} = 0$$
 (32)

Then, the flow velocity v can be obtained from the integral of dv:

$$v = \frac{-\Delta p \cdot r^{D_{T}+1}}{2^{2-D_{T}} L_{0}^{D_{T}} \mu_{0} r_{0}} \left(\frac{r_{0}}{D_{T}+1} - \frac{r}{D_{T}+2} \right) + C$$
 (33)

where C is a constant to be determined. Since the flow velocity v = 0 at the capillary wall, C can be expressed as:

$$C = \frac{\Delta p \cdot r_0^{D_T + 1}}{2^{2 - D_T} L_0^{D_T} \mu_0} \cdot \frac{1}{(D_T + 1)(D_T + 2)}$$
(34)

Substituting Eq. (34) into Eq. (33) gives the expression for flow velocity below:

$$v = \frac{\Delta p}{2^{2 - D_{\rm T}} L_0^{D_{\rm T}} \mu_0} \left(\frac{r_0^{D_{\rm T} + 1}}{(D_{\rm T} + 1)(D_{\rm T} + 2)} - \frac{r^{D_{\rm T} + 1}}{D_{\rm T} + 1} + \frac{r^{D_{\rm T} + 2}}{r_0(D_{\rm T} + 2)} \right)$$
(35)

The flow rate through a single capillary is:

$$q = \int_{0}^{q} dq = \int_{0}^{r_{0}} v dA = \int_{0}^{r_{0}} v \cdot 2\pi r dr$$
 (36)

Substituting Eq. (35) into Eq. (36) yields:

$$q = \frac{\pi \Delta p r_0^{D_{\rm T}+3}}{2^{2-D_{\rm T}} L_0^{D_{\rm T}} \mu_0 (D_{\rm T}+3)(D_{\rm T}+4)}$$
(37)

Eq. (37) indicates that in a capillary with radius r, when tortuosity is not considered ($D_{\rm T}=1$), $q=\pi\Delta pr^4/(40\mu_0L_0)$, meaning that the single-tube flow rate is only 20% of the theoretical value. In fact, considering the effects of tortuosity would further reduce this value. Then, based on Eq. (37), the total flow rate Q through a unit cell can be obtained by summing the flow rates from each individual tube:

$$Q = \sum_{i=1}^{J} q(r_i) = \frac{\pi \Delta p}{2^{2-D_T} L_0^{D_T} \mu_0(D_T + 3)(D_T + 4)} \sum_{i=1}^{J} r_i^{D_T + 3}$$
(38)

where r_i denotes the radius of the *i*-th capillary. Based on Eq. (7) and compared with Darcy's Law yields:

$$A_{\rm p} = \sum_{i=1}^{J} a_i^2 = \sum_{i=1}^{J} \pi r_i^2 \tag{41}$$

where a_i is the cross-sectional area of the i-th capillary based on Eq. (7) for each Monte Carlo simulation. It is evident that when the following convergence criterion is met:

$$A_{I} \ge A_{t} \tag{42}$$

The simulation for this round ends, and the permeability value is recorded. Finally, the average effective permeability <*K*> can be obtained from the following equation:

$$\langle K \rangle = \frac{1}{T} \sum_{i=1}^{T} K_i \tag{43}$$

Here, T represents the total number of Monte Carlo simulations conducted under a given porosity, and K_i is the permeability value output in each simulation. Then, the sample standard deviation can be defined as:

$$s = \sqrt{\frac{1}{T - 1} \sum_{i=1}^{T} (K_i - \overline{K})^2}$$
 (44)

Additionally, based on Eqs. (22) and (37), and according to the principle of equivalent flow, the flow rates of both should be equal, that is:

$$\frac{\pi \Delta p r^{D_{\mathrm{T}}+3}}{2^{2-D_{\mathrm{T}}} L_0^{D_{\mathrm{T}}} \mu_0 (D_{\mathrm{T}}+3) (D_{\mathrm{T}}+4)} = \frac{\pi (r-h)^4 \Delta p}{8 \mu_0 (2r)^{1-D_{\mathrm{T}}} L_0^{D_{\mathrm{T}}}} \tag{45}$$

Thus, the ratio of the boundary layer thickness to the tube radius is:

$$\frac{h}{r} = 1 - \left(\frac{4}{(D_{\rm T} + 3)(D_{\rm T} + 4)}\right)^{\frac{1}{4}} \tag{46}$$

Eq. (46) represents the analytical model for calculating the

$$K = \frac{\pi}{2^{2-D_{T}}} \frac{L_{0}^{1-D_{T}}}{A_{J}} \frac{1}{(D_{T}+3)(D_{T}+4)} \sum_{i=1}^{J} r_{i}^{D_{T}+3} = \frac{\pi}{2^{2-D_{T}}} \frac{L_{0}^{1-D_{T}}}{A_{J}} \frac{1}{(D_{T}+3)(D_{T}+4)} \sum_{i=1}^{J} \left(\frac{r_{\min}}{(1-R_{i})^{1/D_{f}}}\right)^{D_{T}+3}$$
(39)

Eq. (39) is the Fractal-Monte Carlo permeability probability model. The equation contains no empirical constants, and each term has a clear physical meaning. Once the other parameters in the equation are determined, the permeability can be calculated using a Monte Carlo simulation by selecting a set of random numbers R_i . A_j in the equation represents the total cross-sectional area of the unit cell generated using FMCM. According to Eq. (7), each newly generated pore increases the pore area of the unit cell, and A_l correlates with its porosity as follows:

$$A_{\rm J} = \frac{A_{\rm p}}{\phi} = L_0^2 \tag{40}$$

where the pore area $A_{\rm p}$ generated by the probabilistic model is:

thickness of the adsorption layer and contains no empirical parameters. Superficially, h/r appears to be only a function of the tortuosity fractal dimension $D_{\rm T}$. In fact, as shown in Eq. (28), $D_{\rm T}$ is a function of microscopic pore structure parameters such as ϕ , $D_{\rm f}$, $\lambda_{\rm min}$ and $\lambda_{\rm max}$. Therefore, Eq. (46) fully reflects the influence of the reservoir's microscopic pore structure on the boundary layer.

4.2. Supplementary notes

In Section 4.1, we presented the theoretical model for calculating the boundary layer thickness in tight reservoirs (Eq. (46)), and in Section 3, we also provided the semi-empirical formula for the same purpose (Eq. (19)). As mentioned earlier, when the latter is adopted, the formula must be re-fitted using experimental data to determine the two empirical constants. In this case, based on Eqs. (22) and (27), the total flow rate Q through a unit cell with a cross-

sectional area A_J can be obtained by summing the flow rates of individual tubes:

$$Q = \sum_{i=1}^{J} q(r_i) = \sum_{i=1}^{J} \frac{\pi (r_i - h_i)^4 \Delta p}{8\mu (2r_i)^{1 - D_T} L_D^{D_T}}$$
(47)

where h_i denotes boundary layer thickness of the i-th capillary. Substituting Eq. (7) into Eq. (47) and comparing it with Darcy's Law, we can also obtain the permeability of the dense reservoir as follows:

$$K = \frac{\pi}{2^{4-D_{\mathrm{T}}}} \frac{L_0^{1-D_{\mathrm{T}}}}{A_J} \sum_{i=1}^{J} \frac{(r_i - h_i)^4}{r_i^{1-D_{\mathrm{T}}}} = \frac{\pi}{2^{4-D_{\mathrm{T}}}} \frac{L_0^{1-D_{\mathrm{T}}}}{A_J} \sum_{i=1}^{J} \frac{\left(\frac{r_{\min}}{(1-R_i)^{1/D_{\mathrm{f}}}} - h_i\right)^4}{\left(\frac{r_{\min}}{(1-R_i)^{1/D_{\mathrm{f}}}}\right)^{1-D_{\mathrm{T}}}}$$

$$(48)$$

Eq. (48) represents the semi-empirical permeability probability model based on FMCM, where $h_i = ar_i \zeta^b$, with a and b as the fitting parameters. It should be noted that, in addition to using FMCM, an analytical approach can also be directly applied. This is due to the vast number of capillaries/pores within porous media, where the sizes of the pore throats can be considered as continuously distributed. Therefore, the above permeability expression can be directly obtained through integration. That is, the total flow through bundles of capillaries can be expressed as:

Given that $1 < D_T < 3$ and $0 < D_f < 2$, and considering $r_{min}/r_{max} \rightarrow 10^{-2}$ (Yu et al., 2014), Eq. (51) can be simplified to:

$$Q = \frac{\pi \Delta p D_f r_{\text{max}}^{3+D_T}}{2^{2-D_T} L_0^{D_T} \mu_0 (D_T + 3) (D_T + 4) \left(D_T - D_f + 3 \right)}$$
 (52)

Compared with Darcy's Law yields:

$$K = \frac{\pi}{2^{2-D_{\rm T}}} \frac{L_0^{1-D_{\rm T}}}{A} \frac{D_{\rm f} r_{\rm max}^{3+D_{\rm T}}}{(D_{\rm T}+3)(D_{\rm T}+4)(D_{\rm T}-D_{\rm f}+3)}$$
 (53)

Eqs. (50) and (53) represent mono-fractal analytical models for the permeability of tight reservoirs, with each term in the formulas having a clear physical meaning and being suitable for analyzing the factors influencing permeability. Also, both equations indicate a high sensitivity of effective permeability to the maximum capillary radius. Therefore, the accuracy of predictions largely depends on accurately measuring the maximum pore radius. In Section 5.1, we compare the prediction results from the fractal analytical model with those from the FMCM-based probabilistic model (Eq. (39)) that we proposed previously, to highlight the limitations of the mono-fractal theory and the advantages of the numerical simulation method.

4.3. Algorithm for permeability prediction based on FMCM

The algorithm for determining the permeability of tight reservoirs based on FMCM is summarized in the flowchart shown in Fig. 4. The specific steps are summarized as follows:

$$Q = \int_{r_{\min}}^{r_{\max}} q(r)(-dN) = \int_{r_{\min}}^{r_{\max}} \frac{\pi(r-h)^4 \Delta p}{8\mu(2r)^{1-D_T} L_0^{D_T}} D_f r_{\max}^{D_f} r^{-(D_f+1)} dr = \frac{\pi \Delta p D_f r_{\max}^{D_f}}{2^{4-D_T} \mu L_0^{D_T}} \int_{r_{\min}}^{r_{\max}} \frac{(r-h)^4}{r^{D_f+2-D_T}} dr$$

$$(49)$$

According to Darcy's Law yields:

$$K = \frac{\pi}{2^{4-D_{\rm T}}} \frac{L_0^{1-D_{\rm T}}}{A} D_{\rm f} r_{\rm max}^{D_{\rm f}} \int_{r}^{r_{\rm max}} \frac{(r-h)^4}{r^{D_{\rm f}+2-D_{\rm T}}} \mathrm{d}r$$
 (50)

Since the thickness of the boundary layer h depends on the pore radius (as shown in Eq. (19)), the integral formula in Eq. (50) cannot be simplified further. Nevertheless, an approximate permeability value can be obtained through numerical methods. Similarly, in Section 4.1, the total flow through bundles of capillaries in porous media can be also expressed as:

- 1) Given the porosity ϕ , and determine r_{max} and r_{min} based on quantitative characterization experiments of pore structure (such as MICP, NMR, SEM, and CT scanning).
- 2) Determine the fractal dimension D_f and A_t using Eqs. (8) and (9), respectively.
- 3) Generate random numbers $R_i \sim U(0,1)$.
- 4) Calculate r_i using Eq. (7). If $r_i > r_{\text{max}}$, return to step 3 (typically, $r_i < r_{\text{min}}$ is not restricted because its impact on K is minimal).
- 5) Calculate A_p , A_l , and L_0 by Eqs. (41) and (40), respectively.
- 6) Find r_{av} , τ_{av} , and D_T by Eqs. (28), (30) and (31), respectively.
- 7) Calculate the equivalent permeability K using Eq. (39).

$$Q = \int_{r_{min}}^{r_{max}} q(r)(-dN) = \int_{r_{min}}^{r_{max}} \frac{\pi \Delta p r^{D_T + 3}}{2^{2 - D_T} L_0^{D_T} \mu_0(D_T + 3)(D_T + 4)} D_f r_{max}^{D_f} r^{-(D_f + 1)} dr = \frac{\pi \Delta p D_f r_{max}^{3 + D_T}}{2^{2 - D_T} L_0^{D_T} \mu_0(D_T + 3)(D_T + 4) \left(D_T - D_f + 3\right)} \left(1 - \left(\frac{r_{min}}{r_{max}}\right)^{D_T - D_f + 3}\right)$$

$$(51)$$

⁸⁾ Repeat steps 3–7 until Eq. (42) is satisfied, and then record the final value of *K* for one simulation round.

9) Determine the average permeability using Eq. (43).

The above algorithm is straightforward, requiring no grid discretization or complex numerical calculations, and can be run 100,000 times on a personal laptop in just a few minutes.

5. Results and discussions

This section first validates the effectiveness of the proposed models, which is divided into two parts: the first part validates the semi-empirical formula for calculating the thickness of the boundary layer, and the second part validates the permeability model (this part actually covers the validation of the theoretical model for calculating the thickness of boundary flow). Additionally, the effects of different parameters on the boundary layer and permeability of tight reservoirs are examined.

5.1. Model validation

5.1.1. Semi-empirical formula for calculating the thickness of the boundary layer

Four different datasets were used to validate the effectiveness of Eq. (19). Fig. 5 shows a comparison between the proposed model and others, in which the Tian et al. model (2015) is widely adopted for calculating boundary layer thickness. It should be noted that in Fig. 5(b) and (d), some experimental parameters (such as fluid viscosity, density, or average capillary radius) were not provided in the literature. Therefore, to better illustrate the variation in boundary layer thickness and eliminate the impact of differences in experimental conditions on the validation results, we introduced the dimensionless thickness of the boundary layer h^* as follows:

$$h^* = \frac{h}{h_{\text{max}}} \tag{54}$$

where $h_{\rm max}$ represents the calculated maximum thickness of the boundary layer. Similarly, the normalized ratio of the boundary layer thickness to the capillary radius $(h/r)^*$ is defined as:

$$\left(\frac{h}{r}\right)^* = \frac{h/r}{(h/r)_{\text{max}}}\tag{55}$$

where $(h/r)_{\rm max}$ is the maximum value of the ratio of the boundary layer thickness to the capillary radius. Fig. 5 shows that, compared to other models, the proposed semi-empirical model demonstrates superior agreement between the predicted and experimental values. This indicates that the model is highly effective and reliable in calculating the thickness of the adsorption layer under different experimental conditions. To quantitatively evaluate the predictive capability of each model, we calculated the correlation coefficient between the predicted and experimental values, with the detailed results provided in Table 1.

Fig. 5 and Table 1 reveal that when the capillary radius is small, the classical model by Tian et al. (2015) exhibits high accuracy in predicting boundary layer thickness. However, as the capillary radius increases, this model's accuracy declines significantly (as shown in Fig. 5(d)). In contrast, the model by Wang et al. (2020) demonstrates high accuracy in Fig. 5(b), but exhibits relatively large errors in other datasets. This result is expected, as the Wang et al. model (2020) was specifically developed based on the experimental data in Fig. 5(b), making it highly adaptable. However, as a purely empirical formula, this model has limited generalizability and even shows an inverse trend in Fig. 5(d). In comparison, the proposed semi-empirical model shows superior accuracy across various experimental conditions. It is worth noting that both our

model and the Tian et al. (2015) model adopt experimental data from Li et al. (2011) in the process of developing the models. Unlike the DPD simulation approach used by Tian et al. (2015, 2016), the new model was proposed based on a more general dimensional analysis method. This methodology improves the model's robustness, ensuring stable performance despite changes in fluid type, test conditions, or sample characteristics.

5.1.2. Permeability probability model based on FMCM

In previous research, a permeability probability model incorporating boundary layer effect was developed. To validate the model's effectiveness, some typical sand-conglomerate samples were selected for routine core analysis and MICP measurements. Table 2 lists the physical test results for nine rock samples. In the core permeability measurement experiment, the flow rates were controlled between 0.01 and 0.05 mL/min. The MICP experiment shows that the maximum pore throat radius primarily ranged from 0.5 to 4 μm .

Table 3 lists the input and output parameters for a Monte Carlo simulation. Fig. 6 presents the pore radius distribution calculated from the probability model (using Eq. (7) at $\phi = 0.14$), showing that

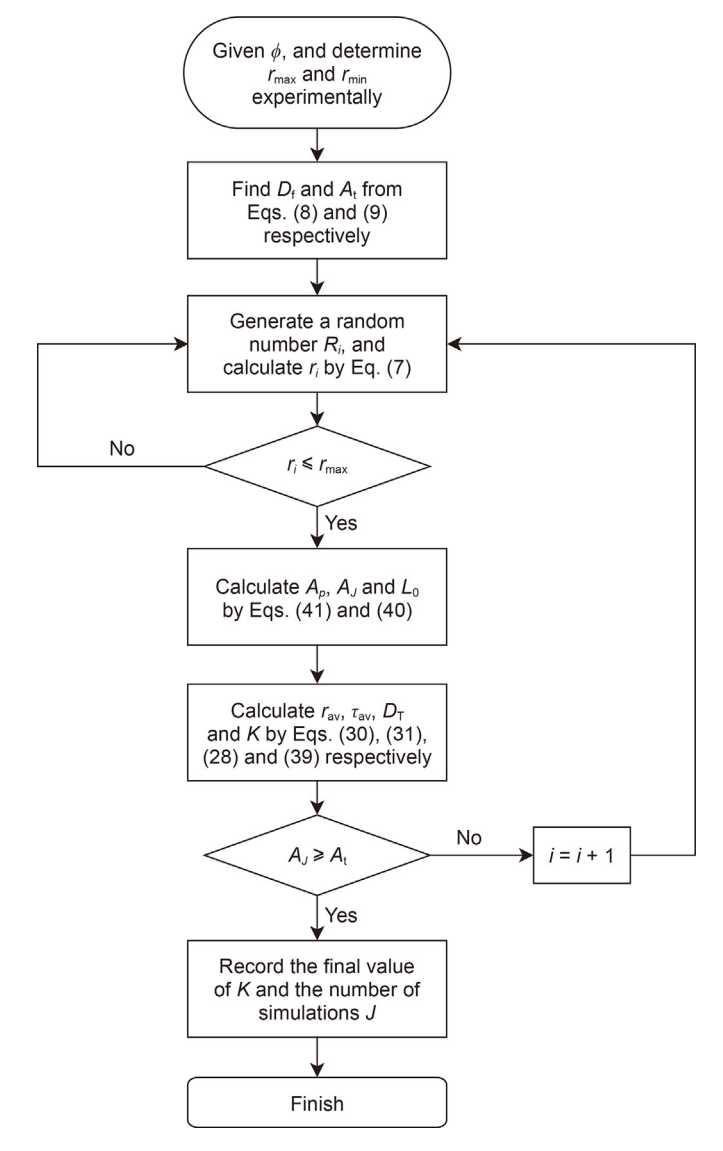


Fig. 4. The flowchart of the Monte Carlo simulation to calculate permeability in fractal porous media.

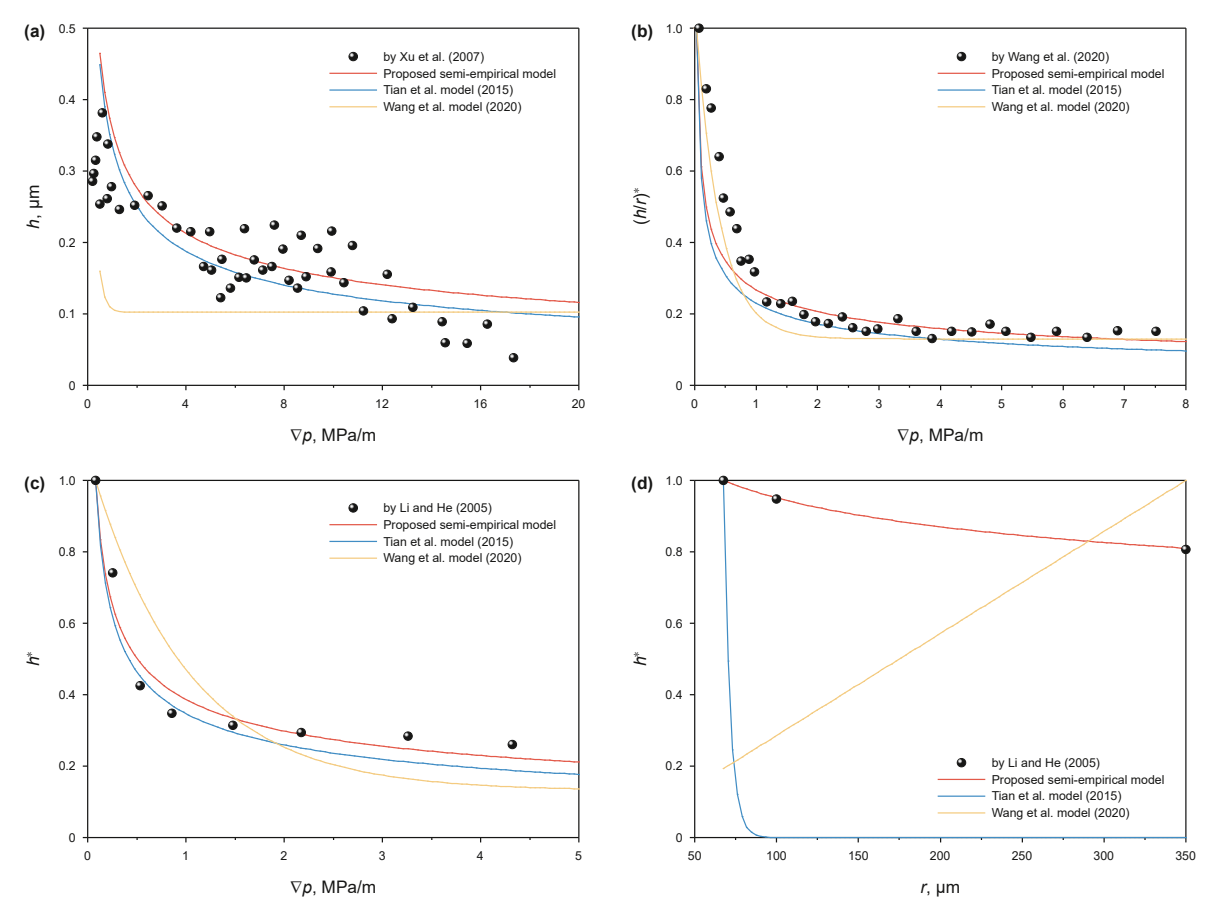


Fig. 5. The predictions using different models and compared with experimental results from various sources. **(a)** The relationship between pressure gradient ∇p and boundary layer thickness $h, r = 2.5 \, \mu m, \rho = 1 \, \text{g/cm}^3, \mu = 1 \, \text{mPa} \cdot \text{s};$ **(b)** The relationship between ∇p and the normalized ratio of boundary layer thickness to capillary radius; **(c)** The relationship between ∇p and normalized boundary layer thickness h^* , $\mu = 5 \, \text{mPa} \cdot \text{s};$ **(d)** The relationship between capillary radius r and h^* , $\nabla p = 0.06 \, \text{MPa/m}, \mu = 2.5 \, \text{mPa} \cdot \text{s}.$

 Table 1

 Correlation coefficients between predictions from different models and experimental data from various sources.

Experimental data source	Correlation coefficients R ²						
	Proposed semi-empirical model	Tian et al. model (2015)	Wang et al. model (2020)				
Xu et al. (2007)	0.789	0.779	0.483				
Wang et al. (2020)	0.968	0.965	0.985				
Li and He (2005)	0.981	0.982	0.912				
Li and He (2005)	0.999	0.707	-0.988				

Table 2Core conventional analysis results.

Core No.	Length, cm	Diameter, cm	Maximum pore radius, μm	Minimum pore radius, μm	Porosity, %	Permeability, mD
1	4.691	2.520	0.92	0.0063	7.7	0.12
2	4.878	2.515	1.21	0.0063	8.6	0.35
3	4.782	3.660	1.47	0.0063	9.8	0.44
4	3.091	3.665	1.92	0.0063	9.5	0.66
5	3.933	3.780	2.13	0.0063	11.2	1.14
6	4.590	2.520	2.45	0.0063	12.1	1.56
7	3.211	3.640	2.84	0.0063	13.2	2.21
8	4.950	2.525	3.96	0.0063	9.9	3.27
9	4.384	3.800	3.68	0.0063	14.0	4.22

the number of larger pores is significantly less than that of smaller pores, which is consistent with the basic theory of fractal geometry.

Fig. 7 displays the distribution of equivalent permeability K values obtained from 1000 Monte Carlo simulations at a porosity of $\phi=0.14$. It is observed that the simulated K values fluctuate around

an average of 4.55 mD, which is expected due to the randomness in pore size distribution. Thus, we consider 4.55 mD as the equivalent permeability value for the sample under a specific number of simulations.

Table 3
Input and output parameters of the model in one Monte Carlo simulation and their descriptions.

Model Parameter		Value	Description
Input	$\phi \ r_{ m max} \ r_{ m min} \ T$	14.0% 3.68 μm 0.0063 μm 1000	Porosity Maximum pore radius Minimum pore radius Number of simulations
output	$egin{array}{l} D_{ m f} & & & & & & & & & & & & & & & & & & $	1.69 1432.15 μm² 236.32 μm² 1688.00 μm² 41.08 μm 0.0154 μm 3.96 1.19 0.021 54985 4.55 mD 2.681	Pore fractal dimension Cross-sectional area of the cubic REV Generated cumulative pore area Total cross-sectional area of the generated unit cell Edge length of the generated unit cell Average capillary radius Average tortuosity Average tortuosity fractal dimension Dimensionless number Total number of pores generated in one simulation Equivalent permeability Standard deviation

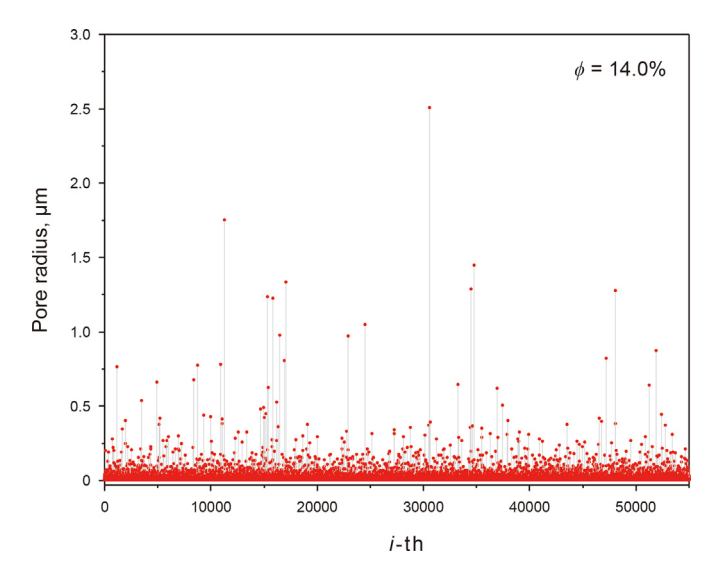


Fig. 6. The pore radius distribution generated based on FMCM in one simulation at porosity $\phi=14\%$.

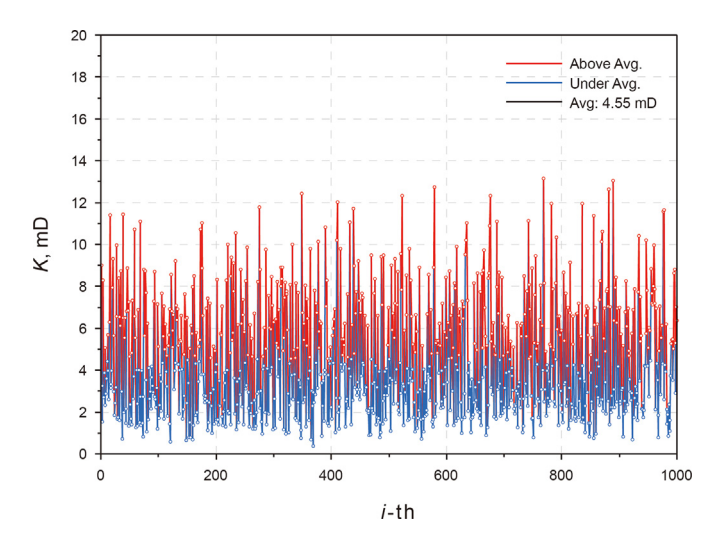


Fig. 7. The effective permeability predicted using FMCM in 1000 runs of simulations.

Table 4 lists the effective permeability and standard deviation for four typical samples at different simulation counts. It is clear that when the total number of runs T exceeds 10,000, the effective permeability values converge, becoming nearly identical to those at T=100,000. Therefore, in subsequent work, we consistently use T=10,000 as the number of simulations. Table 4 and Fig. 7 show that although pore sizes are randomly selected and permeability predictions fluctuate, performing a sufficient number of simulations leads to convergent values.

To validate the effectiveness of the Fractal-Monte Carlo model, the predictive capabilities of different models for the permeability of tight rocks were compared (Fig. 8). Table 5 presents the relative errors between the calculated and measured values for different models.

Among these, Yu model (2016) is the classic Fractal-Monte Carlo model. Although this model demonstrates high accuracy in predicting permeability in high-permeability reservoirs (Yu, 2016; Yu et al., 2005), as shown in Fig. 8 and Tables 5 and it completely fails in low-permeability reservoirs. The large computational errors further suggest that the boundary layer effect is a key factor influencing the permeability of tight reservoirs. The models by Wang et al. (2017) and Huang et al. (2018) are fractal analytical models that account for the boundary layer effect in tight reservoirs. In their models, the determination of boundary layer thickness still follows the classic Tian et al. (2015) model. As discussed in Section 5.1.1. the accuracy of the boundary layer thickness calculated by Tian et al. (2015) decreases with increasing pore radius. A similar trend is also observed in Fig. 8, where increasing sample permeability (and average pore radius) leads to higher calculation errors in the Wang et al. (2017) and Huang et al. (2018) models, with the maximum relative error exceeding 200%. In contrast, the effective permeability calculated by the proposed probabilistic model is closest to the measured value, with the smallest relative error.

Nevertheless, an objective fact is that the relative error of the new model remains relatively large, with a few data points exceeding 20%. This error is attributed to three main factors. First, the permeability measurement experiment is influenced by various factors that can cause fluctuations in the results. These factors include human errors during the experiment, equipment calibration accuracy, variations in environmental conditions, as well as the heterogeneity and compactness of the samples. Due to these various influencing effects, achieving complete accuracy and

reliability in permeability measurements is challenging, especially for tight core samples, where precise measurements are even more difficult. Secondly, during the MICP experiment, samples with a matrix-supported fine-grained gravel lithology (e.g., samples 1 and 4) may experience crack formation. Matrix-supported fine-grained gravel consists of small gravel, clay minerals, and sandstone particles. When subjected to high pressure, the relatively weak cohesion between the matrix and particles, especially in the gaps between fine gravel particles, increases the probability of deformation or rupture during the high-pressure mercury injection process. Additionally, the particles themselves may undergo local yielding or failure under high pressure, causing cracks to extend not only along the surface and edges of the particles, but also into their interior, forming various types such as gravel-crossing, gravelboundary, and intra-gravel cracks (Zhou et al., 2021). As a result, the maximum pore radius derived from the MICP experiment may be overestimated, limiting the predictive capability of the model. Third, the low permeability of the samples (with an average permeability of only 1.5 mD) also affects the model predictions. It is known that for high permeability samples, small absolute deviations (e.g., a slight change in a single decimal place) typically lead to small relative errors, which are often negligible. However, for low permeability samples, the same absolute deviations result in much larger relative errors, which can notably impact the accuracy of the results. In this case, the average relative errors of other models are remarkably large, at 68.2%, 121.3%, and 525.9%, respectively. In contrast, the proposed model demonstrates a high degree of accuracy, with a much lower average relative error of only 14.4%, significantly smaller than that of other existing models. Therefore, given the relatively small absolute errors, we consider the average relative error of 14.4% for the proposed model to be

It should be noted that Table 5 also presents the prediction performance of the derived fractal analytical model (Eq. (53)). Although the absolute and relative errors of this analytical model are considerably smaller than those of other published models, its prediction accuracy is still lower than that of the fractal probability model, further confirming the superiority of the latter. As mentioned in Section 4.2, the accuracy of the analytical model's predictions largely depends on precise measurement of the maximum pore radius, and even slight measurement errors can cause fluctuations in permeability values. In contrast, the proposed probability model simultaneously considers the fractal and random distributions of capillary sizes in real porous media. To some extent, the "randomness" helps mitigate the impact of measurement errors in the maximum pore radius. This explains why the Fractal-Monte Carlo method was chosen for permeability simulation in this study.

5.2. Sensitivity analysis of influencing parameters

A series of parameter sensitivity analyses was conducted to quantitatively assess the impact of various parameters on the simulation results. When evaluating the influence of a specific parameter on the predicted outcomes, other parameters are kept constant. This section focuses on examining the factors that affect the thickness of boundary flow and effective permeability.

5.2.1. Influence analysis of boundary layer thickness

In this work, a semi-empirical model (Eq. (19)) and an analytical model (Eq. (46)) were proposed for calculating the boundary layer thickness in Sections 3 and 4.1, respectively. In this part, we first analyze the influencing factors based on the semi-empirical model. Fig. 9 reveals the effects of specific mechanical and geometric parameters on the thickness of the boundary layer within capillaries. Fig. 9(a) and Eq. (19) indicate that with a fixed fluid type, an increase in pressure gradient leads to a thinner boundary layer, thus reducing the ratio h/r. As the pressure gradient increases to a certain level, the thickness of the boundary layer gradually stabilizes. This occurs because at low pressure gradient, the shear forces between fluids are insufficient to overcome the adhesion of the pore throat walls and the intermolecular forces among the fluid molecules. Consequently, this results in significant percolation resistance, leading to a thicker boundary layer. As the pressure gradient increases, the shear forces between fluids also increase, gradually reducing the thickness of the boundary layer (Huang et al., 2018). Fig. 9(b) shows that the thickness of the boundary layer decreases with increasing capillary radius and gradually stabilizes. This is because the smaller the tube radius, the stronger the nonlinearity of the flow, and the greater the proportion of the boundary fluid (Li, 2010).

Fluid viscosity also plays a key role in the development of the boundary layer. Fig. 9(c) shows that under constant density and pressure gradient, higher viscosity typically increases the boundary layer thickness, resulting in a higher h/r ratio. This is because a higher viscosity indicates a greater proportion of polar molecules in the fluid, which makes the fluid more likely to adhere to the walls

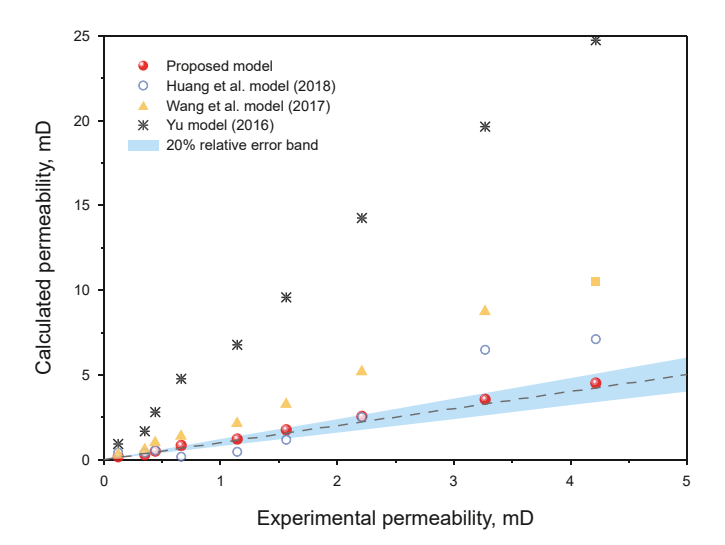


Fig. 8. Comparison between permeability results by experimental test and model calculations.

Table 4 Effective permeability K and standard deviation s under different simulation runs.

Sample porosity, %	T = 100		T = 1000		T = 10,000		T = 100,000	
	K, mD	S	K, mD	S	K, mD	S	K, mD	S
14.0	4.646	2.884	4.551	2.681	4.512	2.639	4.523	2.632
12.1	1.675	1.052	1.792	1.028	1.758	1.044	1.754	1.045
9.8	0.542	0.333	0.511	0.310	0.510	0.308	0.510	0.308
7.7	0.153	0.099	0.153	0.091	0.149	0.093	0.151	0.094

Table 5Comparison of calculated and experimental permeability for different models with relative error.

Core No.	Exp., mD	Proposed probability model		Huang et al. model (2018)		Wang et al. model (2017)		Yu (2016) model		Fractal analytical model (Eq. (53))	
		Calc., mD	Rel. Error, %	Calc., mD	Rel. Error, %	Calc., mD	Rel. Error, %	Calc., mD	Rel. Error, %	Calc., mD	Rel. Error, %
1	0.12	0.149	24.2	0.403	235.8	0.283	135.8	0.91	658.3	0.153	27.5
2	0.35	0.301	14.0	0.411	17.4	0.595	70.0	1.66	374.3	0.302	13.7
3	0.44	0.510	15.9	0.524	19.1	1.024	132.7	2.81	538.6	0.517	17.5
4	0.66	0.822	24.5	0.158	76.1	1.366	107.0	4.76	621.2	0.838	27.0
5	1.14	1.223	7.3	0.465	59.2	2.126	86.5	6.77	493.9	1.239	8.7
6	1.56	1.758	12.7	1.159	25.7	3.267	109.4	9.57	513.5	1.772	13.6
7	2.21	2.545	15.2	2.503	13.3	5.178	134.3	14.27	545.7	2.593	17.3
8	3.27	3.546	8.4	6.485	98.3	8.72	166.7	19.66	501.2	3.582	9.5
9	4.22	4.512	7.0	7.115	68.7	10.525	149.5	24.75	486.8	4.547	7.8

of the pore throats, thus increasing the thickness of the boundary layer. Fig. 9(c) and Eq. (19) demonstrate that the ratio h/r is nearly linearly related to μ ($h/r \propto \mu$ ^{0.752}), which is consistent with the findings reported by Li and He (2005), Tian et al. (2015, 2016), and Meng et al. (2018).

Fluid density affects the momentum of the fluid, thereby influencing the development of the boundary layer. Fig. 9(d) reveals that under constant viscosity and pressure gradient, higher density may lead to a thinner boundary layer. This is because the increased inertial forces are able to overcome a certain amount of viscous force, allowing more boundary fluid to participate in the flow. Compared to other influencing factors, the impact of fluid density on the boundary layer fluid is relatively mild.

Combining Fig. 9(a)—(d), it is evident that the smaller the capillary radius, the greater the sensitivity of the boundary layer thickness to changes in different parameters. As the capillary radius increases, the rate of change in the boundary layer (steepness of the curve) gradually decreases. This explains why the impact of the boundary layer can be neglected in conventional reservoirs, but not in tight reservoirs. Therefore, it is reasonable to conclude that the dimensionless number ζ in Eq. (19) encompasses most mechanisms affecting the thickness of the boundary layer.

Additionally, Fig. 10 analyzes the impact of various microscopic pore structure parameters on the boundary layer, as described by Eq. (46). Fig. 10(a) shows the effect of the average tortuosity fractal dimension on boundary layer thickness for different capillary radii.

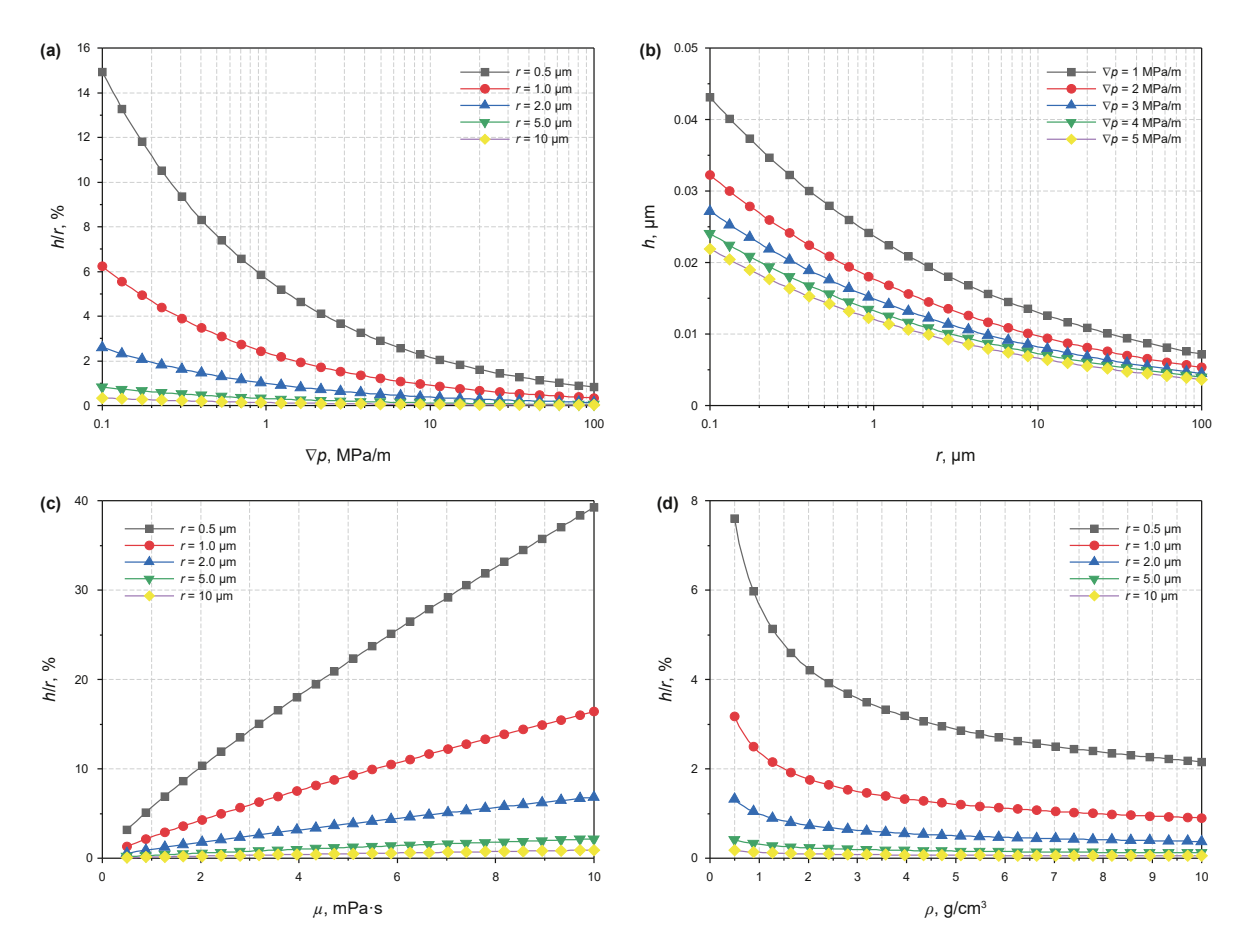


Fig. 9. Analysis of the factors affecting boundary layer thickness based on Eq. (19). (a) The effect of pressure gradient ∇p on the ratio of boundary layer thickness to capillary radius h/r under different tube radii r, $\rho=1$ g/cm³, $\mu=1$ mPa·s; (b) The effect of r on boundary layer thickness r under different r, $\rho=1$ g/cm³, $\rho=1$ mPa·s; (c) The effect of fluid viscosity $\rho=1$ mPa·s, $\rho=1$ g/cm³, $\rho=1$ mPa/m; (d) The effect of fluid density $\rho=1$ mPa·s, $\rho=1$ mPa·s, $\rho=1$ mPa/m.

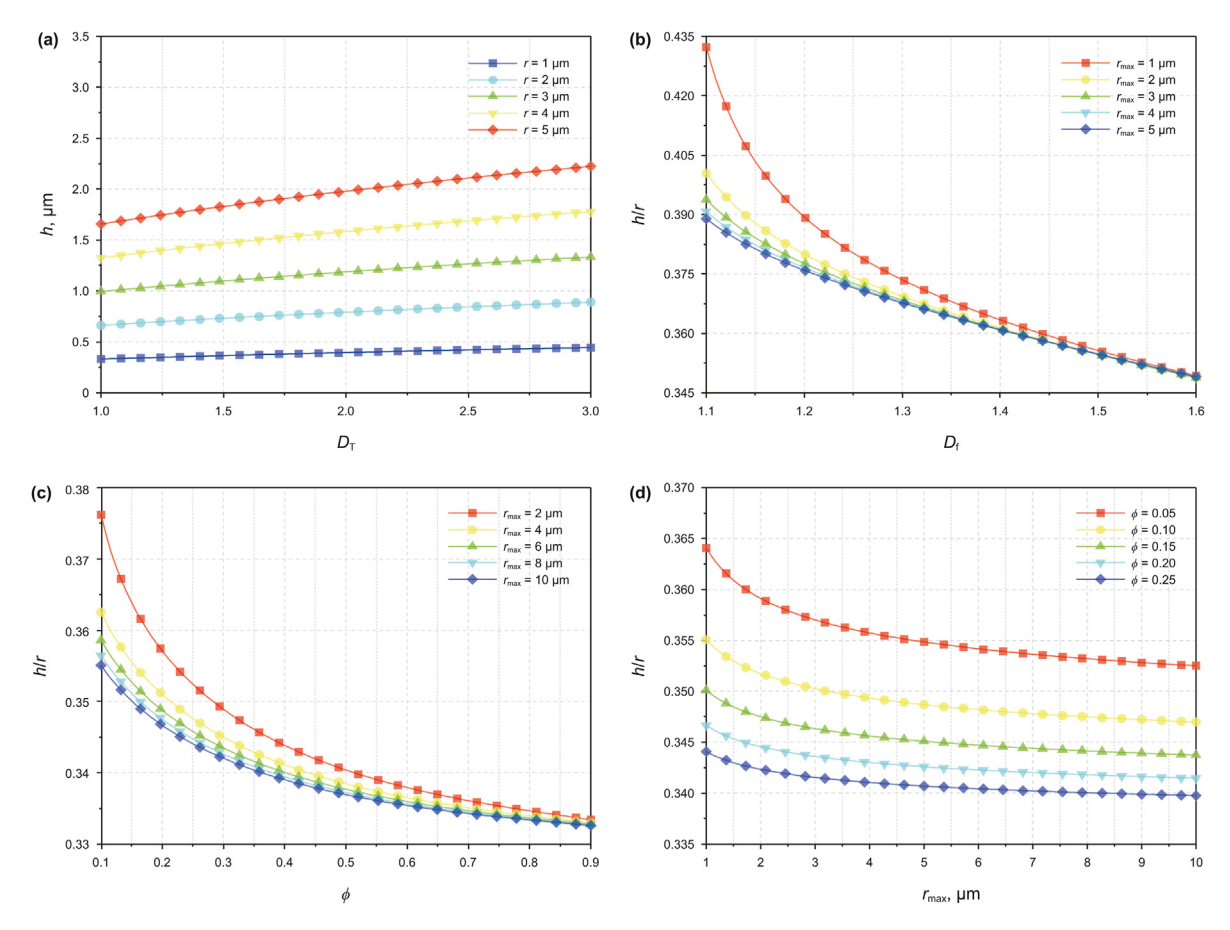


Fig. 10. Analysis of the factors affecting boundary layer thickness based on Eq. (56). (a) The effect of average tortuosity fractal dimension D_T on boundary layer thickness h under different capillary radii r; (b) The effect of fractal dimension D_T on the ratio of boundary layer thickness to capillary radius h/r under different maximum pore radii r_{max} $r_{\text{min}} = 0.1 \ \mu\text{m}$; (c) The effect of porosity ϕ on h/r under different r_{max} $r_{\text{min}} = 0.1 \ \mu\text{m}$; (d) The effect of r_{max} on h/r under different ϕ , $r_{\text{min}} = 0.01 \ \mu\text{m}$.

The results indicate that the boundary layer thickness increases with the tortuosity fractal dimension. This is because a higher tortuosity fractal dimension corresponds to more tortuous flow paths, which significantly increase the specific surface area of the reservoir. The larger specific surface area leads to enhanced interactions between solid and liquid molecules, increasing flow resistance and resulting in a thicker boundary layer.

Fig. 10(b) illustrates that a higher fractal dimension results in a thinner boundary layer. A larger fractal dimension increases the pore-filling capacity in the porous media and the probability of connectivity between the flow paths. Therefore, the increased complexity of the pore structure facilitates smoother fluid flow, reducing the thickness of boundary flow. It is also observed that when the fractal dimension exceeds 1.5, the five curves nearly coincide. This occurs because, when the fractal dimension is lower, the number of pores and the porosity are relatively low (Yu et al., 2014). In this case, the largest pore in the porous media plays a positive role in reducing overall flow resistance. However, as the fractal dimension increases, the number of pores increases sharply, and the influence of the single largest flow path on flow resistance diminishes. Therefore, when $D_{\rm f}$ reaches a certain value, the variation of h/r with $D_{\rm f}$ is no longer affected by the maximum pore radius.

Fig. 10(c) shows a negative correlation between h/r and porosity. This is expected because, according to Eq. (8), porosity is positively correlated with $D_{\rm f}$, and its influence on the boundary layer follows a similar trend to that of $D_{\rm f}$. Specifically, greater pore space facilitates fluid flow, reducing the boundary layer effect. In addition, Fig. 10(d) shows that for dense media (i.e., low porosity), an increase in

maximum pore diameter significantly reduces fluid-wall interaction in the initial stage, thereby enhancing overall permeability. However, for non-dense media (i.e., high porosity), due to the larger average pore size and good pore connectivity, the boundary layer effect is relatively mild. As a result, the effect of maximum pore radius on the boundary layer is minimal. The above findings reveal how the reservoir's microscopic pore structure affects the boundary layer effect.

5.2.2. Influence analysis of permeability

The mechanical parameters discussed in Section 5.2.1 are not reiterated in Section 5.2.2, as their effects on the thickness of the boundary layer and permeability are exactly opposite. Fig. 11 reveals the influence patterns of additional physical and geometric parameters on the fluid flow characteristics within capillaries.

The maximum capillary radius $r_{\rm max}$ is a critical parameter in the probability model. Given $r_{\rm max}$, $r_{\rm min}$, and porosity ϕ , the fractal dimension $D_{\rm f}$ and pore size distribution of the porous media can be determined. Fig. 11(a) shows the relationship between effective permeability and maximum pore radius under different porosities. It indicates that, with other parameters held constant, effective permeability increases rapidly as the maximum capillary radius increases. This is because, on one hand, an increase in $r_{\rm max}$ leads to a higher total number of capillaries within the porous media, significantly enhancing the reservoir's percolation capacity. On the other hand, as $r_{\rm max}$ rises, the impact of the boundary layer gradually decreases (as shown in Fig. 10(d)).

Fig. 11(b) illustrates the relationship between effective permeability and porosity at different maximum pore radii. As shown in

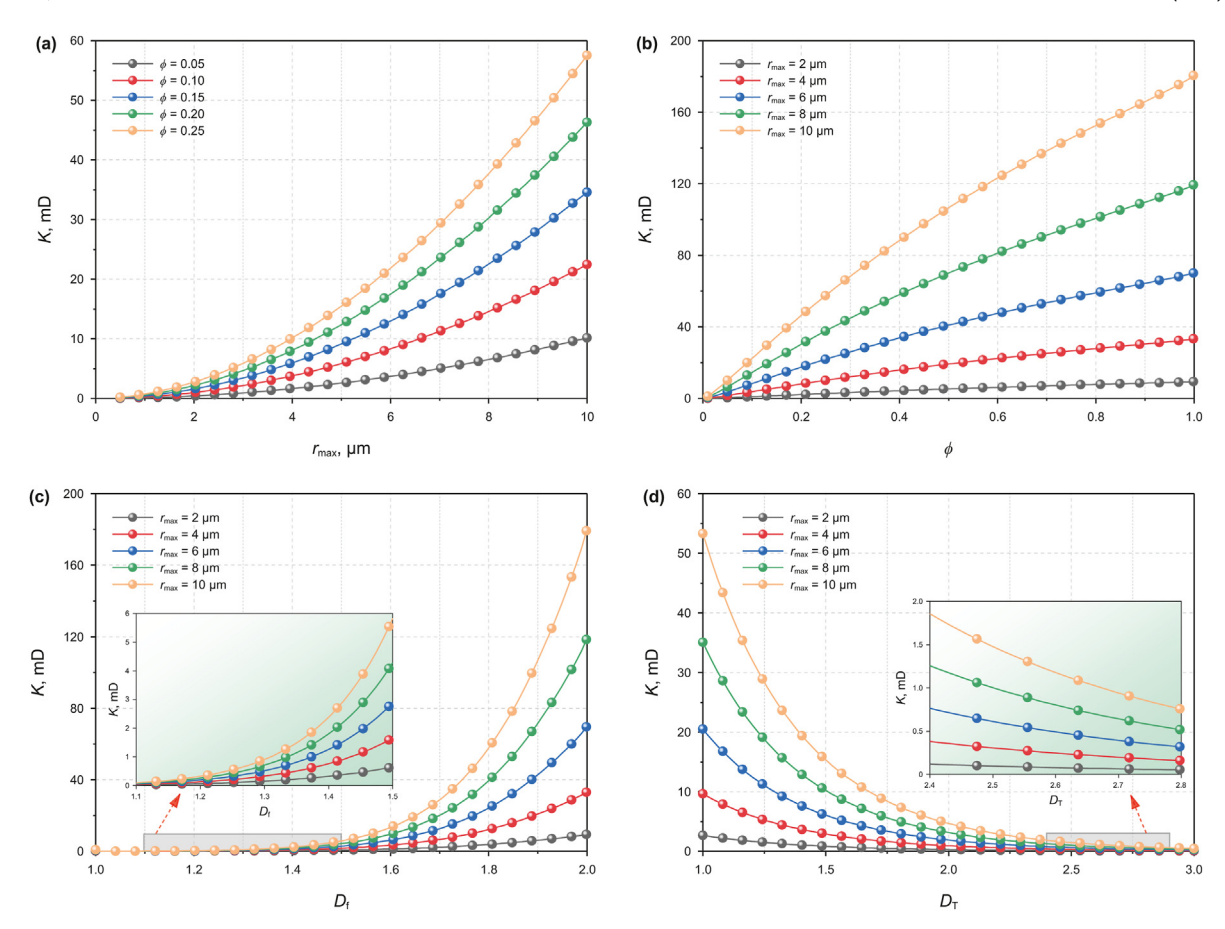


Fig. 11. Analysis of the factors affecting permeability, $r_{\min} = 0.01 \ \mu m$. (a) The effect of maximum pore radius r_{\max} on permeability K under different porosity ϕ ; (b) The effect of ϕ on K under different r_{\max} ; (c) The effect of fractal dimension D_T on K under different r_{\max} ; (d) The effect of average tortuosity fractal dimension D_T on K under different r_{\max} , $\phi = 15\%$.

the figure, the positive correlation between permeability and porosity is a commonly observed fact. The mechanism by which porosity affects permeability is multifaceted. First, as noted in the previous section, porosity is positively correlated with the fractal dimension. According to Eq. (8), in the limiting case, when porosity ϕ approaches 1, D_f reaches its maximum value of 2 (in a 2D plane). Therefore, higher porosity indicates better pore development, leading to improved flow performance. Second, from Eq. (28), it can be concluded that $D_{\rm T}$ decreases as ϕ increases. As ϕ approaches 1, the medium contains almost no matrix particles, and the flow paths become straight, causing $D_{\rm T}$ to reach its minimum value of 1. In contrast, as ϕ decreases, the number of matrix particles in the medium gradually increases, increasing the curvature of the flow paths and flow resistance. Additionally, it can be observed that, at the same porosity, the media with a larger r_{max} exhibit stronger percolation capabilities, which is expected.

Fig. 11(c) shows the relationship between effective permeability and $D_{\rm f}$ at different maximum pore radii. As previously mentioned, the magnitude of $D_{\rm f}$ reflects the development of the reservoir's porosity. An increase in $D_{\rm f}$ leads to a higher total number of capillaries, which in turn enhances the effective permeability, consistent with previous research findings (Lahiri, 2021; Wu et al., 2022; Zhou and Zhao, 2020). It should be noted that permeability is generally positively correlated with the pore fractal dimension, rather than the particle fractal dimension. An increase in the particle fractal dimension results in greater complexity in the pore structure, which subsequently leads to a decrease in permeability. Therefore, it is essential to clearly distinguish the object of study when determining fractal dimensions.

The effect of $D_{\rm T}$ on effective permeability is illustrated in Fig. 11(d). Clearly, a larger $D_{\rm T}$ indicates greater heterogeneity in the reservoir, resulting in a reduction in the permeability of the porous media. The figure also shows that the rate of permeability decrease with $D_{\rm T}$ is related to the parameter $r_{\rm max}$. Specifically, the larger the $r_{\rm max}$, the greater both the rate and extent of permeability decline. This is because, in dense reservoirs, the contribution of numerous nano-scale pores to permeability is minimal, whereas the relatively few micron-scale pores serve as the primary flow spaces and contribute the majority of the permeability (Lai et al., 2015).

6. Conclusions

In this paper, semi-empirical and theoretical models for the boundary layer thickness of tight reservoirs are established based on experimental data and fractal theory, respectively. Subsequently, permeability predictions are conducted using Monte Carlo simulations. Based on this, the influence mechanisms of various parameters on the boundary layer and effective permeability are systematically studied. These analyses provide insights into how the physical properties and geometric configurations of the reservoir affect fluid flow characteristics within capillaries. The related conclusions are as follows:

(1) Compared to the existing formulas commonly used to calculate the thickness of the boundary layer, the semiempirical formula proposed through dimensional analysis offers higher computational accuracy and broader applicability. The model integrates various mechanical, physical, and

geometric parameters influencing the boundary layer into a dimensionless number, with fewer empirical constants than the classical formulas, enabling it to better reflect the mechanisms affecting the thickness of the boundary fluid.

- (2) Compared to large pores, the boundary layer effect in small pores is more pronounced and cannot be ignored. The boundary layer thickness decreases with increasing pressure gradient, capillary size, and fluid density, while it shows an approximately linear positive correlation with fluid viscosity. Furthermore, it is found that pore structure parameters also have a significant impact on the boundary layer. A larger tortuosity fractal dimension results in a thicker boundary layer, while increases in pore fractal dimension, porosity, and maximum capillary size reduce the boundary layer effect.
- (3) The non-flow boundary layer can significantly reduce the effective permeability of tight formations. Permeability is positively correlated with the maximum pore radius, porosity, and pore fractal dimension, and negatively correlated with the tortuosity fractal dimension. Sensitivity analysis reveals that the impact of different pore structure parameters on the permeability of large pores is much greater than that on small pores. This indicates that the development of the relatively few large pores is a key factor in improving overall permeability.
- (4) In predicting the permeability for tight reservoir, the proposed Fractal-Monte Carlo probabilistic model exhibits higher computational accuracy than the theoretical model based on mono-fractal theory. This indicates that combining fractal geometry with the Monte Carlo method can expand the application scope of fractal theory, offering an effective approach to studying transport mechanisms in tight porous media.
- (5) Compared to traditional numerical algorithms, the current Fractal-Monte Carlo simulation technique is not constrained by grid generation, equation discretization, or boundary condition settings. It is characterized by ease of implementation and low computational effort. Future research may focus on the following directions: First, the simulation algorithm may be further improved to reduce variance and enhance computational accuracy; Second, this technique could be extended to analyze other transport properties of porous media, such as thermal and electrical conductivity, to improve its versatility and applicability in practical applications.

CRediT authorship contribution statement

You Zhou: Writing — original draft. **Song-Tao Wu:** Writing — review & editing. **Ru-Kai Zhu:** Investigation. **Xiao-Hua Jiang:** Investigation. **Gan-Lin Hua:** Formal analysis.

Declaration of competing interest

The authors declare that they have no known competing financial interests or personal relationships that could have appeared to influence the work reported in this paper.

Acknowledgments

This work was financially supported by the Hebei Provincial Natural Science Foundation of China (No. D2023402012) and the Major Science and Technology Project of China National Petroleum Corporation (No. 2024DI87).

Nomenclature

riomener	uturt
a_i	Cross-sectional area of the <i>i</i> -th capillary (μ m ²)
A_I	Total cross-sectional area of the generated unit cell
J	(μm^2)
$A_{\rm p}$	Generated cumulative pore area (μm^2)
A_{t}^{p}	Cross-sectional area of the cubic REV (µm²)
ď	Euclidean dimension
D_{f}	Pore fractal dimension
D_{T}	Average tortuosity fractal dimension
$f(\lambda)$	Probability density function (PDF)
h	Boundary layer thickness (µm)
h_{max}	Maximum thickness of the boundary layer
h_i	Boundary layer thickness of the <i>i</i> -th capillary (μm)
h*	Dimensionless thickness of the boundary layer
h/r	Ratio of the boundary layer thickness to the capillary
	radius
$(h/r)_{max}$	Maximum ratio of the boundary layer thickness to the
	capillary radius
(h/r)*	Normalized ratio of the boundary layer thickness to the
	capillary radius
J	Total number of capillaries generated in one simulation
K	Permeability (mD)
< <i>K</i> >	Average effective permeability (mD)
K_i	The <i>i</i> -th permeability (mD)
L_0	Edge length of the generated unit cell (μm)
L_{t}	Actual length of the curved capillary (μm)
N	Number of capillary tubes
Q	Total flow rate through a unit cell $(10^{-9} \text{ m}^3/\text{s})$
q(r)	Flow rate through a single capillary of radius $r(10^{-9} \text{ m}^3/\text{ m}^3)$
	s)
R	Random number
Re	Reynolds number
R_i	The <i>i</i> -th random number
$R(\lambda)$	Cumulative distribution function (CDF)
r	Pore radius (µm)
r_{av}	Average capillary radius (µm)
r_i	The <i>i</i> -th capillary radius (μm)
S	standard deviation
T	Total number of simulations
v	Flow velocity (m/s)
λ	Pore diameter (µm)
λ_{\min}	Minimum pore diameter (μm)
λ_{\max}	Maximum pore diameter (μm)
φ	Porosity (%)
μ	Fluid viscosity (mPa·s)
μ_0	Fluid inherent viscosity (mPa·s)
ρ	Fluid density (g/cm³) Dimensionless number
ζ	
$ au_{ m av}$	Average capillary diameter (um)
λ _{av}	Average capillary diameter (µm)
∇p	Pressure gradient (MPa/m) Driving pressure difference (MPa)
Δp	
CT DPD	Computed tomography dissipative particle dynamics
MAPS	
MICP	Modular automated processing system Mercury injection capillary pressure
IVIII P	WEIGHT INTECTION CONTINCT NECCTIFE

Appendix A. Supplementary data

Supplementary data to this article can be found online at https://doi.org/10.1016/j.petsci.2025.04.016.

Mercury injection capillary pressure

Nuclear magnetic resonance

Scanning electron microscope

MICP

NMR

SEM

References

- Abbasi, M.A., Ezulike, D.O., Dehghanpour, H., et al., 2014. A comparative study of flowback rate and pressure transient behavior in multifractured horizontal wells completed in tight gas and oil reservoirs. J. Nat. Gas Sci. Eng. 17, 82–93. https://doi.org/10.1016/j.jngse.2013.12.007.
- Ablimit, I., Tang, Y., Cao, J., et al., 2016. Accumulation mechanism and enrichment rules of the continuous hydrocarbon plays in the lower triassic baikouquan formation of the Mahu Sag, Junggar Basin. Nat. Gas Geosci. 27 (2), 241–250. https://doi.org/10.11764/j.issn.1672-1926.2016.02.0241 (in Chinese).
- Behmanesh, H., Hamdi, H., Clarkson, C.R., et al., 2018. Analytical modeling of linear flow in single-phase tight oil and tight gas reservoirs. J. Pet. Sci. Eng. 171, 1084–1098. https://doi.org/10.1016/j.petrol.2018.08.023.
- Cai, J.C., Xia, Y.X., Lu, C., et al., 2020. Creeping microstructure and fractal permeability model of natural gas hydrate reservoir. Mar. Petrol. Geol. 115, 104282. https://doi.org/10.1016/j.marpetgeo.2020.104282.
- Cao, R.Y., Wang, Y., Cheng, L.S., et al., 2016. A new model for determining the effective permeability of tight formation. Transport Porous Media 112, 21–37. https://doi.org/10.1007/s11242-016-0623-0.
- Chen, A.M., Miao, T.J., Li, Z., et al., 2022a. Fractal Monte Carlo simulations of the effective permeability for a fracture network. Fractals 30 (4), 2250074. https://doi.org/10.1142/S0218348X22500748.
- Chen, H., Xing, J.P., Jiang, D.L., et al., 2022b. A fractal model of low-velocity non-Darcy flow considering viscosity distribution and boundary layer effect. Fractals 30 (1), 2250006. https://doi.org/10.1142/S0218348X22500062.
- Du, M., Xiang, Y., Jia, N.H., et al., 2021. Pore structure characteristics of tight glutenite reservoirs of Baikouquan Formation in Mahu Sag. Lithol. Reservoirs 32 (5), 120–131. https://doi.org/10.12108/yxyqc.20210511 (in Chinese).
- Ge, J.L., Liu, Y.T., Yao, Y.D., 2003. The Modern Mechanics of Fluids Flow in Oil Reservoir. Petroleum Industry Press (in Chinese).
- Guo, B.E., Xiao, N., Martyushev, D., et al., 2024. Deep learning-based pore network generation: numerical insights into pore geometry effects on microstructural fluid flow behaviors of unconventional resources. Energy 294, 130990. https:// doi.org/10.1016/j.energy.2024.130990.
- Huang, S., 2022. Mechanism and Application of Transient Inter-porosity Flow between Matrix and Fracture in Tight Oil Reservoirs. Ph.D. dissertation, China University of Petroleum (Beijing). https://doi.org/10.27643/d.cnki.g-sybu.2019.001838 (in Chinese).
- Huang, S., Yao, Y.D., Zhang, S., et al., 2018. A fractal model for oil transport in tight porous media. Transport Porous Media 121, 725–739. https://doi.org/10.1007/ s11242-017-0982-1.
- Kuang, H., Liu, H., Tan, X.F., et al., 2023. Study on factors affecting the petro physical properties of sandstone and conglomerate reservoirs of Baikouquan Formation, Junggar Basin. Front. Earth Sci. 10, 1033344. https://doi.org/10.3389/ faut. 2022.1033344
- Kulga, B., Ertekin, T., 2018. Numerical representation of multi-component gas flow in stimulated shale reservoirs. J. Nat. Gas Sci. Eng. 56, 579–592. https://doi.org/ 10.1016/j.jngse.2018.06.023.
- Lahiri, S., 2021. Estimating effective permeability using connectivity and branch length distribution of fracture network. J. Struct. Geol. 146, 104314. https:// doi.org/10.1016/j.jsg.2021.104314.
- Lai, J., Wang, G.W., Meng, C.Q., et al., 2015. Pore structure characteristics and formation mechanisms analysis of tight gas sandstones. Prog. Geophys. 30 (1), 217–227. https://doi.org/10.6038/pg20150133 (in Chinese).
- Li, Z.Y., Lei, Z.D., Shen, W.J., et al., 2023b. A comprehensive review of the oil flow mechanism and numerical simulations in shale oil reservoirs. Energies 16 (8), 3516. https://doi.org/10.3390/en16083516.
- Li, B.W., Sun, L.H., Liu, X.G., et al., 2023a. Effects of clay mineral content and types on pore-throat structure and interface properties of the conglomerate reservoir: a case study of Baikouquan Formation in the Junggar Basin. Minerals 13 (1), 9. https://doi.org/10.3390/min13010009.
- Li, J., Tang, Y., Wu, T., et al., 2020. Overpressure origin and its effects on petroleum accumulation in the conglomerate oil province in Mahu Sag, Junggar Basin, NW China. Petrol. Explor. Dev. 47 (4), 679–690. https://doi.org/10.11698/ PED.2020.04.04 (in Chinese).
- Li, X.Y., Ji, H.C., Chen, L., et al., 2022. Hydraulic fractures evaluation of the glutenite and the effects of gravel heterogeneity based on cores. Int. J. Rock Mech. Min. Sci. 160, 105264. https://doi.org/10.1016/j.jirmms.2022.105264.
- Li, Y., 2010. Study of Microscale Nonlinear Flow Characteristics and Flow Resistance Reducing Methods. Ph.D. dissertation, Chinese Academy of Sciences (in Chinese).
- Li, Y., Lei, Q., Liu, X.G., et al., 2011. Characteristics of micro scale nonlinear filtration. Petrol. Explor. Dev. 38 (3), 336–340. https://doi.org/10.1016/S1876-3804(11) 60036-0.
- Li, Z.F., He, S.L., 2005. Influence of boundary layers upon filtration law in low-permeability oil reservoirs. Daqing Pet. Geol. Dev. 24 (2), 57–59+77 (in Chinese).
- Liu, D.X., Yue, X.A., Yan, S., et al., 2005. Influential mechanism of adsorbed water layers on percolation in low permeability oil reservoir. Pet. Geol. Recovery Eff. 12 (6), 40–42 (in Chinese).
- Liu, H.B., Cui, S., Meng, Y.F., et al., 2022. Study on rock mechanical properties and wellbore stability of fractured carbonate formation based on fractal geometry. ACS Omega 7 (47), 43022–43035. https://doi.org/10.1021/acsomega.2c05270.

Liu, H.Q., Xie, H.P., Wu, F., et al., 2024. A novel box-counting method for quantitative fractal analysis of three-dimensional pore characteristics in sandstone. Int. J. Min. Sci. Technol. 34 (4), 479–489. https://doi.org/10.1016/j.ijmst.2024.04.006.

- Meng, Z., Yang, S.L., Wang, L., et al., 2018. A new optimization and correction method for measuring the thickness of boundary layer in a tight reservoir. J. Petrochem. Univ. 31 (2), 65–69+100. https://doi.org/10.3969/j.issn.1006-396X.2018.02.012 (in Chinese).
- Peng, S.C., Deng, Y., Li, Y.Y., et al., 2024. An enhanced presence of tricyclic terpanes in the Triassic oils from the tight conglomerate reservoir in the Mahu Sag, Junggar Basin, NW China. Petrol. Sci. Technol. https://doi.org/10.1080/ 10916466.2024.2430300.
- Shang, Z.H., Dong, L., Niu, L.S., et al., 2019. Adsorption of methane, nitrogen, and carbon dioxide in atomic-scale fractal nanopores by Monte Carlo simulation I: single-component adsorption. Energy Fuels 33 (11), 10457–10475. https://doi.org/10.1021/acs.energyfuels.9b01405.
- Tan, F.Q., Ma, C.M., Zhang, X.Y., et al., 2022. Migration rule of crude oil in microscopic pore throat of the low-permeability conglomerate reservoir in Mahu Sag, Junggar Basin. Energies 15 (19), 7359. https://doi.org/10.3390/en15197359.
- Tian, W.C., Lu, S.F., Huang, W.B., et al., 2019. Study on the full-range pore size distribution and the movable oil distribution in glutenite. Energy Fuels 33 (8), 7028–7042. https://doi.org/10.1021/acs.energyfuels.9b00999.
- Tian, X.F., Cheng, L.S., Li, X.L., et al., 2014. A new method to calculate relative permeability considering the effect of pore-throat distribution. J. Shaanxi Univ. Sci. Technol. Nat. Sci. Ed. 32 (6), 100–104 (in Chinese).
- Tian, X.F., Cheng, L.S., Yan, Y.Q., et al., 2015. An improved solution to estimate relative permeability in tight oil reservoirs. J. Pet. Explor. Prod. Technol. 5, 305–314. https://doi.org/10.1007/s13202-014-0129-7.
- Tian, X.F., Cheng, L.S., Cao, R.Y., et al., 2016. Characteristics of boundary layer in micro and nano throats of tight sandstone oil reservoirs. Chin. J. Comput. Phys. 33 (6), 717–725. https://doi.org/10.19596/j.cnki.1001-246x.2016.06.011 (in Chinese).
- Wang, F.Y., Fu, J., 2021. A fractal model for apparent liquid permeability of dual wettability shale coupling boundary layer and slip effect. Fractals 29 (4), 2150088. https://doi.org/10.1142/S0218348X21500882.
- Wang, F.Y., Liu, Z.C., Jiao, L., et al., 2017. A fractal permeability model coupling boundary-layer effect for tight oil reservoirs. Fractals 25 (5), 1750042. https:// doi.org/10.1142/S0218348X17500426.
- Wang, H.L., Tian, L., Gu, D.H., et al., 2020. Method for calculating non-Darcy flow permeability in tight oil reservoir. Transport Porous Media 133, 357–372. https://doi.org/10.1007/s11242-020-01427-8.
- Wang, Q.Y., Liu, G.N., Cheng, G.J., et al., 2025. A multi-field coupled fractal model for shale gas extraction considering water reflux and microstructure evolution. Phys. Fluids 37, 013326. https://doi.org/10.1063/5.0246269.
- Wang, X.W., Yang, Z.M., Qi, Y.D., et al., 2011. Effect of absorption boundary layer on nonlinear flow in low permeability porous media. J. Cent. South Univ. Technol. 18, 1299–1303. https://doi.org/10.1007/s11771-011-0836-x.
- Wang, Z.Q., Ge, H.K., Zhou, W., et al., 2022. Characterization of pores and micro-fractures in tight conglomerate reservoirs. Int. J. Hydrogen Energy 47 (63), 26901–26914. https://doi.org/10.1016/j.ijhydene.2022.06.037.
- Wu, J.B., Yang, S.L., Gan, B.W., et al., 2021. Pore structure and movable fluid characteristics of typical sedimentary lithofacies in a tight conglomerate reservoir, Mahu Depression, Northwest China. ACS Omega 6, 23243–23261. https://doi.org/10.1021/acsomega.1c02952.
- Wu, Z.W., Cui, C.Z., Yang, Y., et al., 2022. A fractal permeability model of tight oil reservoirs considering the effects of multiple factors. Fractal Fract 6, 153. https://doi.org/10.3390/fractalfract6030153.
- Xiao, B.Q., Fan, J.T., Ding, F., 2012. Prediction of relative permeability of unsaturated porous media based on fractal theory and Monte Carlo simulation. Energy Fuels 26 (11), 6971–6978. https://doi.org/10.1021/ef3013322.
- Xiao, B.Q., Wang, S.A., Wang, Y., et al., 2020. Effective thermal conductivity of porous media with roughened surfaces by fractal-Monte Carlo simulations. Fractals 28 (2), 2050029. https://doi.org/10.1142/S0218348X20500292.
- Xiao, M., Wu, S.T., Yuan, X.J., et al., 2021. Conglomerate reservoir pore evolution characteristics and favorable area prediction: a case study of the Lower Triassic Baikouquan Formation in the Northwest Margin of the Junggar Basin, China. J. Earth Sci. 32 (4), 998–1010. https://doi.org/10.1007/s12583-020-1083-6.
- Xiong, Y., Yu, J.B., Sun, H.X., et al., 2017. A new non-Darcy flow model for low-velocity multiphase flow in tight reservoirs. Transport Porous Media 117, 367–383. https://doi.org/10.1007/s11242-017-0838-8.
- Xu, P., Wang, J.L., Xu, Y., et al., 2023. Reconstruction of random fibrous porous material and numerical study on its transport properties by fractal Monte Carlo method. Fractals 31 (5), 2350043. https://doi.org/10.1142/S0218348X23500433.
- Xu, S.L., Yue, X.A., Hou, J.R., et al., 2007. Influence of boundary-layer fluid on the seepage characteristic of low-permeability reservoir. J. Xi'an Shiyou Univ. (Nat. Sci. Ed.) 22 (2), 26–28 (in Chinese).
- Yang, J.H., Wang, M., Wu, L., 2021. A novel Monte Carlo simulation on gas flow in fractal shale reservoir. Energy 236, 121513. https://doi.org/10.1016/ j.energy.2021.121513.
- Yang, Z., Zou, C.N., Hou, L.H., et al., 2019. Division of fine-grained rocks and selection of "sweet sections" in the oldest continental shale in China: taking the coexisting combination of tight and shale oil in the Permian Junggar Basin. Mar. Petrol. Geol. 109, 339–348. https://doi.org/10.1016/j.marpetgeo.2019.06.010.
- Yin, Z.Z., Zheng, Q., Wang, H.L., et al., 2022. Effective gas diffusion coefficient of fractal porous media with rough surfaces by Monte Carlo simulations. Fractals 30 (1), 2250010. https://doi.org/10.1142/S0218348X22500104.

- Yu, B.M., 2016. A mini-review on the Fractal-Monte Carlo method and its applications in porous media. Sixth International Conference on Porous Media and its Applications in Science, Engineering and Industry. http://dc.engconfintl.org/porous_media_vi/24.
- Yu, B.M., Cheng, P., 2002. A fractal permeability model for bi-dispersed porous media. Int. J. Heat Mass Tran. 45, 2983—2993. https://doi.org/10.1016/S0017-9310(02)00014-5.
- Yu, B.M., Lee, L.J., Cao, H.Q., 2002. A fractal in-plane permeability model for fabrics.
 Polym. Compos. 23 (2), 201–221. https://doi.org/10.1002/pc.10426.
 Yu, B.M., Li, J.H., 2001. Some fractal characters of porous media. Fractals 9 (3),
- Yu, B.M., Li, J.H., 2001. Some fractal characters of porous media. Fractals 9 (3) 365–372. https://doi.org/10.1142/S0218348X01000804.
- Yu, B.M., Li, J.H., 2004. A geometry model for tortuosity of flow path in porous media. Chin. Phys. Lett. 21 (8), 1569–1571. https://doi.org/10.1088/0256-307X/ 21/8/044
- Yu, B.M., Zou, M.Q., Feng, Y.J., 2005. Permeability of fractal porous media by Monte Carlo simulations. Int. J. Heat Mass Tran. 48, 2787–2794. https://doi.org/ 10.1016/j.ijheatmasstransfer.2005.02.008.
- Yu, B.M., Xu, P., Zou, M.Q., 2014. Transport Physics in Fractal Porous Media. Science Press (in Chinese).
- Yu, Z.C., Wang, Z.Z., Adenutsi, C.D., 2023a. Genesis of authigenic clay minerals and their impacts on reservoir quality in tight conglomerate reservoirs of the Triassic Baikouquan formation in the Mahu Sag, Junggar Basin, Western China. Mar. Petrol. Geol. 148, 106041. https://doi.org/10.1016/j.marpetgeo.2022.106041.
- Yu, Z.C., Wang, Z.Z., Lin, W., et al., 2023b. Permeability prediction of tight conglomerates by integrating fractal characteristics and seismic meme inversion: a case study from the Triassic Baikouquan Formation, Junggar Basin, Western China. Fractals 31 (10), 2340010. https://doi.org/10.1142/S0218348X23400108.

- Yuan, X.G., Chang, T.Q., Li, S., et al., 2024. Sedimentary texture differences between lithofacies types and their control on the physical property in fan-delta conglomerate reservoirs: a case study from the Triassic Baikouquan Formation in Mahu Sag, Junggar Basin, Northwestern China. Geoenergy Sci. Eng. 233, 212455. https://doi.org/10.1016/j.geoen.2023.212455.
- Zhang, D.Y., Hu, H.S., Dong, Y., et al., 2023. Seepage simulation of conglomerate reservoir based on digital core: a case study of the Baikouquan Formation in Mahu Sag, Junggar Basin. Processes 11, 3185. https://doi.org/10.3390/pr11113185.
- Zhang, Y.D., Gao, J., Xiao, B.Q., et al., 2024a. A fractal-Monte Carlo approach to simulate Kozeny—Carman constant of roughened fibrous porous media. Fractals 32 (1), 2240113. https://doi.org/10.1142/S0218348X22401132.
- Zhang, Z., Liu, G.F., Liu, H., et al., 2024b. Fractal characterization on methane adsorption in coal molecular structure. Phys. Fluids 36 (12), 126611. https://doi.org/10.1063/5.0231934.
- Zheng, J.Y., Tian, W.C., Gao, Y., et al., 2023. Multi-scale fractal characteristics of the pore system in low-permeability conglomerates from the Junggar Basin. Processes 11, 2667. https://doi.org/10.3390/pr11092667.
- Zhou, X.P., Zhao, Z., 2020. Digital evaluation of nanoscale-pore shale fractal dimension with microstructural insights into shale permeability. J. Nat. Gas Sci. Eng. 75, 103137. https://doi.org/10.1016/j.jngse.2019.103137.
- Zhou, Y., Wu, S.T., Li, Z.P., et al., 2018. Multifractal study of three-dimensional pore structure of sand-conglomerate reservoir based on CT images. Energy Fuels 32 (4), 4797–4807. https://doi.org/10.1021/acs.energyfuels.8b00057.
- Zhou, Y., Wu, S.T., Li, Z.P., et al., 2021. Investigation of microscopic pore structure and permeability prediction in sand-conglomerate reservoirs. J. Earth Sci. 32 (4), 818–827. https://doi.org/10.1007/s12583-020-1082-7.